Research Square

Preprints are preliminary reports that have not undergone peer review.
They should not be considered conclusive, used to inform clinical practice,
or referenced by the media as validated information.

A three-dimensional flexible multibody framework for transient dynamics and wear assessment of sucker-rod systems in directional wells

Yunlong Liu
China University of Petroleum-Beijing at Karamay
Yanlong Zhao
zhaoyanlong@cupk.edu.cn

China University of Petroleum-Beijing at Karamay

Research Article

Keywords: Flexible multibody dynamics, Geometrically exact beam theory, Directional sucker-rod systems, Stress-wave propagation, Rod–tubing contact, Wear assessment

Posted Date: November 25th, 2026

DOI: https://doi.org/10.21203/rs.3.rs-11440675/v1

License: This work is licensed under a Creative Commons Attribution 4.0 International License.
Read Full License

Additional Declarations: No competing interests reported.

A three-dimensional flexible multibody framework for transient dynamics and wear assessment of sucker-rod systems in directional wells

Yunlong Liu[a], Yanlong Zhao[a, *]

a School of Petroleum, China University of Petroleum-Beijing at Karamay, Karamay 834000, China; 2024216900@st.cupk.edu.cn (Y.L.)

* Correspondence: zhaoyanlong@cupk.edu.cn; Tel.: +86-18010092639

Abstract

Directional sucker-rod systems exhibit coupled axial and transverse dynamics, intermittent rod–tubing contact, and spatially localized wear. This study develops a full-scale three-dimensional flexible multibody model for analysing these interactions in a directional well. The rod string is represented using geometrically exact beam theory with finite-volume-based spatial discretization; distributed fluid inertia and squeeze-film resistance, regularized rod–tubing contact and friction, pump loading, and a reduced-order electromechanical drive boundary are coupled in an implicit differential-algebraic formulation implemented in MBDyn. The model is calibrated against the measured surface dynamometer card of a 1707-m directional well. The computed stress-wave propagation and depth-dependent response reveal changes in load transmission associated with rod-section transitions, wellbore curvature, and the transition from tension-dominated to compression-dominated behaviour. An energy-based wear relation maps cycle-resolved contact work to local wear depth and estimates the remaining time to a through-wall criterion. The predicted high-wear region is near the recorded tubing perforation depth, providing case-specific field corroboration of wear localization. A constant-voltage baseline and a modelled adaptive voltage-modulation scenario illustrate a trade-off between reduction of peak tensile loading and high-frequency response under delayed feedback. Centralizer layouts are assessed as geometric interventions that alter local clearance and contact conditions. The framework links full-well transient mechanics to spatial wear assessment, with quantitative life estimates interpreted for the investigated operating conditions.

Keywords

Flexible multibody dynamics; Geometrically exact beam theory; Directional sucker-rod systems; Stress-wave propagation; Rod–tubing contact; Wear assessment

1. Introduction

Sucker rod strings deployed in directional wells are subjected to complex dynamic loads during long-term operation. Compared with vertical wells, curved well trajectories introduce additional geometric constraints and lateral interactions between the rod string and tubing, resulting in transverse vibration, intermittent contact, and eccentric wear [1-3]. These dynamic behaviors can accelerate fatigue damage and reduce the service reliability of sucker rod systems [4]. Therefore, accurately predicting transient responses and identifying the mechanisms governing wear localization are essential for improving the operational safety and maintenance efficiency of directional well production systems.

Existing studies have addressed sucker-rod dynamics in deviated wells, rod–tubing interaction, and wear prediction [5–8]. Models based on one-dimensional rod equations, equivalent-vibration descriptions, and finite-element or finite-difference approaches have provided useful insights into load transmission and downhole response. However, accurately resolving within a single transient simulation the combined effects of three-dimensional rod geometry, stress-wave propagation, evolving rod–tubing contact, fluid resistance, and a compliant electromechanical drive boundary remains challenging. The main issue is not that these physical mechanisms have never been modelled individually, but that their coupled influence on full-well dynamics and spatial wear localization requires further investigation within an integrated computational framework.

Flexible multibody dynamics provides an effective framework for describing the large deformation and spatial motion of slender structures [9]. Among various formulations, Geometrically Exact Beam Theory (GEBT) has been widely adopted for flexible components

undergoing large rotations and nonlinear deformation [10,11]. Recent Cosserat rod formulations have further extended the capability of modelling spatial slender structures with complex constraints [12-14]. Open-source flexible multibody platforms such as MBDyn have been applied to coupled multiphysics simulations involving flexible structures and external fields [15]. Recent engineering applications have demonstrated the capability of flexible multibody approaches in analyzing large-scale coupled dynamic systems, including hydro elastic structures and renewable energy systems [16-18]. Nevertheless, applying flexible multibody approaches to full-scale sucker rod systems remains challenging because the governing equations involve strong coupling between structural deformation, fluid loading, contact interaction, and electromechanical boundary conditions. In addition, the high-frequency transient response associated with stress wave propagation requires an appropriate spatial discretization strategy to maintain numerical accuracy while keeping the computational cost acceptable for engineering-scale simulations.

The surface drive system also plays an important role in determining the dynamic response of sucker rod strings [19]. Different driving conditions, such as constant-voltage operation and adaptive voltage modulation, modify the transmission of dynamic loads from the surface to the downhole structure. Variable-speed drive technologies have been widely investigated in beam pumping systems for improving energy efficiency and operational performance [20]. Recent studies have further emphasized the importance of electromechanical coupling in transient vibration analysis of drivetrain systems [21]. However, the relationship between electromechanical drive characteristics, transient vibration behavior, and fatigue evolution remains insufficiently understood. In particular, whether drive-induced load regulation can compensate for vibration-related damage mechanisms requires further investigation.

This study implements a full-scale three-dimensional flexible multibody model for the investigated directional sucker-rod system in MBDyn. The formulation couples geometrically exact beam dynamics and finite-volume-based spatial discretization with distributed fluid

loading, regularized rod–tubing contact and friction, pump loading, and a reduced-order electromechanical drive boundary. The contribution lies in their system-level integration and in the resulting analysis of transient load transmission, stress-wave propagation, depth-dependent contact behavior, and spatial wear localization. The model is calibrated against the measured surface dynamometer card of the case well, and the predicted wear-prone region is compared with the recorded tubing-failure location. Centralizer placement is then assessed as a geometric intervention that changes local contact conditions. The resulting wear-life estimates are interpreted for the specified operating condition and the adopted wear and failure criteria.

2. System description and numerical implementation

2.1 Full-scale well configuration and operating conditions

To demonstrate the engineering applicability of the proposed framework, a representative directional oil well from an active oilfield block was selected as a field benchmark case. The selected well provides realistic operating conditions, including complex wellbore trajectory, tapered sucker rod configuration, fluid characteristics, and recorded maintenance information, enabling comprehensive evaluation of the proposed failure prediction methodology. The proposed framework is not intended as an empirical statistical predictor calibrated for a specific well, but as a physics-based methodology applicable to directional sucker rod systems under different geological and operational conditions. The nominal pump setting depth for this well is 1707.0 m. To accurately capture the nonlinear modulation effects of the wellbore trajectory on the rod string normal contact forces and spatial friction, the model integrates 51 sets of 3D survey data from the field, utilizing cubic spline interpolation to map these onto the dynamic discretization nodes to ensure curvature continuity [22].

A five-stage tapered sucker rod string configuration is adopted to handle the substantial axial and lateral combined loads characteristic of directional wells. From the surface to the bottom, the rod string consists of high-strength steel sections with diameters of 25 mm (466.0 m), 22 mm (301.0 m), 19 mm (868.0 m), 22 mm (46.0 m), and 19 mm (26.0 m). Correspondingly, the

tubing system undergoes diameter changes at a depth of 1099.0 m, where the internal diameter reduces from 62.0 mm to 54.8 mm.

The produced liquid is represented by prescribed effective fluid properties based on the field reports. The fluid density is set to 950 kg/m³, the dynamic viscosity to 0.02 Pa·s, and the yield stress to 7.5 Pa. These properties enter the distributed fluid-loading and axial-resistance terms described in Section 3.2. The present formulation provides an effective representation of the fluid forces but does not explicitly resolve transient gas–liquid phase distribution or multiphase flow in the rod–tubing annulus.

During the simulation, two modelled drive-boundary conditions are considered: a constant-voltage baseline representing the field-like operating condition and an adaptive asynchronous voltage modulation (AAVM) scenario introduced for numerical comparison. The AAVM case is used to investigate how a prescribed voltage-feedback law interacts with transient rod-string dynamics; it is not intended to reproduce a verified controller installed on the case well. Both simulations use consistent prescribed start-up settings so that the effects of the drive-boundary formulation can be compared.

2.2 Numerical workflow and simulation procedure

The numerical simulation procedure consists of model preparation, computational implementation, transient dynamic solution, and post-processing for fatigue and wear assessment. The overall workflow is established based on the open-source multibody dynamics platform MBDyn, which is customized and extended for the simulation of sucker rod systems in directional wells.

The simulation begins with the preparation of the full-scale well configuration and operating conditions, including well trajectory, sucker rod and tubing geometries, material properties, fluid parameters, and surface driving conditions. The measured-depth-dependent spatial information is discretized to construct the three-dimensional computational representation of the sucker rod string.

The corresponding structural, contact, and loading parameters are then assigned to the multibody model.

To adapt MBDyn for the present petroleum engineering application, a dedicated computational environment is configured, and the source code is modified and recompiled to incorporate the required modeling components. Based on the developed theoretical formulation, the customized MBDyn framework integrates the geometrically exact beam representation, distributed fluid loading, rod-tubing contact interaction, and electromechanical boundary excitation into a unified dynamic simulation framework. This implementation enables the analysis of full-scale sucker rod systems under realistic operational conditions.

During transient simulation, the coupled nonlinear dynamic equations are solved using an implicit time integration procedure. At each time step, the structural deformation, contact evolution, fluid loading, and driving excitation are updated simultaneously, and nonlinear iterations are performed until convergence is achieved. The calculated responses provide the time-dependent evolution of displacement, velocity, stress, contact force, and energy dissipation during sucker rod operation.

Finally, the simulated transient responses are post-processed to evaluate vibration characteristics, wear localization, and fatigue performance. Stress histories and contact-related quantities are extracted to calculate fatigue indicators and remaining useful life. The predicted damage distribution is subsequently used to guide the centralizer optimization strategy for improving the operational reliability of sucker rod systems.

3. Multibody formulation and numerical solution

3.1 Three-dimensional flexible multibody formulation

This study employs the Redundant Coordinate Formulation to abstract the surface pumping unit as a spatial multi-rigid-body system. Under this framework, each moving component is assigned an independent structural node endowed with six degrees of freedom. To rigorously

describe the spatial configuration, the state of an arbitrary node i is defined by its absolute position vector $\mathbf{x}_i \in \mathrm{R}3$ and its orientation matrix $\mathbf{R}_i \in SO(3)$. To circumvent the singularity issues inherent in traditional Euler angles during large-scale rotations, the orientation is parameterized utilizing the rotation vector ϕ based on the Gibbs-Rodrigues formula [23]:

$$R_i = I + \sin\phi\, n\times + (1-\cos\phi) n\times n\times, \tag{1}$$

where ϕ is the magnitude of the rotation, n is the unit vector of the rotation axis, and $n\times$ denotes the skew-symmetric tensor. Accordingly, the virtual perturbation of the orientation is exactly updated via $\delta\mathbf{R}_i = \boldsymbol{\theta}_{i\delta} \times \mathbf{R}_i$, where $\boldsymbol{\theta}_{i\delta}$ characterizes the virtual rotation vector.

Based on the MBDyn absolute coordinate formulation, the dynamic equilibrium of the i-th structural node is governed by the exact Newton-Euler equations. The momentum $\boldsymbol{\beta_i}$ and momenta moment $\boldsymbol{\gamma_i}$ of the node, which inherently incorporate the varying mass distribution, are formulated as:

$$\beta_i = m(\dot{x}_\iota + \omega_i \times s_i), \tag{2}$$

$$\gamma_i = s_i \times \dot{x}_\iota + J_i \omega_i, \tag{3}$$

where $\boldsymbol{s_i}$ is the static moment with respect to the node position, and $\boldsymbol{J_i}$ is the inertia tensor. The contribution of the node to the global equilibrium is defined by the time derivatives of these momenta:

$$\dot{\beta}_\iota = f_{in}, \tag{4}$$

$$\dot{\gamma}_\iota + \dot{x}_\iota \times \beta_i = m_{in}, \tag{5}$$

where $\boldsymbol{f_{in}}$ and $\boldsymbol{m_{in}}$ represent the external generalized forces and moments applied to the node.

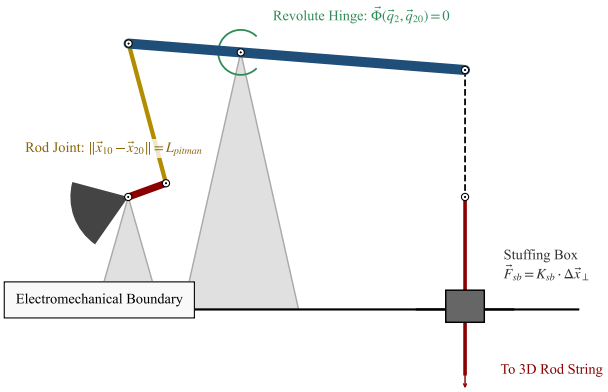


Fig. 1. Multibody kinematic topology and electromechanical boundary of the surface pumping unit. The integration of the Redundant Coordinate Formulation with a compliant motor model replaces conventional rigid kinematic constraints, enabling the effective

absorption of transient stress wave reflections and ensuring the numerical stability of the DAE solver.

The spatial topological relationships of the mechanism are defined by the algebraic constraint equations $\boldsymbol{\Phi}(\boldsymbol{q},t) = 0$. For core articulated joints, such as the crank main shaft and the walking beam pivot, revolute hinge constraints are formulated. A revolute hinge between node i and node j intrinsically restricts five relative degrees of freedom by enforcing the coincidence of the attachment points and the parallelism of the respective local rotational axes. The holonomic constraint equations are mathematically expressed as:

$$\begin{cases} \mathrm{x_i} + \mathrm{R_i d_i} - \left(\mathrm{x_j} + \mathrm{R_j d_j}\right) = \mathbf{0} \\ \left(\mathrm{R_i e_{3i}}\right)^{\mathrm{T}}\left(\mathrm{R_j e_{2j}}\right) = \mathbf{0} \\ \left(\mathrm{R_i e_{3i}}\right)^{\mathrm{T}}\left(\mathrm{R_j e_{1j}}\right) = \mathbf{0} \end{cases}, \tag{6}$$

where $\mathbf{d_i}$ and $\mathbf{d_j}$ denote the constant offset vectors in the respective local frames, and $\mathbf{e}_k$ represents the unit basis vectors. These constraints are appended to the system dynamic equations using Lagrange multipliers $\boldsymbol{\lambda}$.

Based on this kinematic topology, the instantaneous pose of the crank pin is driven by the superposition of the active electromagnetic torque and the gravitational torque of the counterweight. The equivalent balance torque $\mathrm{T_{bal}}$ generated by the counterweight on the crank main shaft follows:

$$\mathrm{T_{bal}} = \mathrm{M_{bal}} \cdot g \cdot \mathrm{R_{bal}} \cdot \sin(\theta + \phi), \tag{7}$$

where θ is the instantaneous rotation angle of the crank, $\mathrm{M_{bal}}$ is the mass of the counterweight, $\mathrm{R_{bal}}$ is the rotation radius of the center of gravity of the counterweight, and ϕ is the phase angle.

At the surface wellhead, the polished rod is radially restricted by a stuffing box. To avoid over-constrained phenomena and the resultant Jacobian matrix singularities typically caused by rigid kinematic constraints, this study employs a penalty-based deformable displacement joint. The relative distance vector $\tilde{\boldsymbol{d}}$ and its objective relative velocity $\dot{\tilde{\boldsymbol{d}}}$ projected in the reference frame of the wellhead are derived as:

$$\tilde{d} = R_w^T\left(x_p - x_w\right), \tag{8}$$

$$\dot{\tilde{d}} = R_w^T\left(\dot{x_p} - \dot{x_w} - \omega_w \times \left(x_p - x_w\right)\right), \tag{9}$$

where subscript p refers to the polished rod node. Consequently, the mechanical response of the stuffing box is formulated through a linear viscoelastic constitutive law applied specifically to the transverse plane [24]:

$$F_{sb} = K_{sb}\widetilde{d_\perp} + C_{sb}\dot{\tilde{d}}_\perp, \tag{10}$$

where the transverse constraint stiffness is set to $K_{sb} = \mathrm{diag}(10^9, 10^9, 0)\mathrm{N/m}$. By imposing the virtual work $\delta \boldsymbol{L_{sb}} = \delta \tilde{\boldsymbol{d}}^T \boldsymbol{F_{sb}}$, this penalty formulation effectively ensures the radial alignment of the polished rod while mathematically providing a minimal elastic clearance, thereby enhancing the global convergence robustness of the high-dimensional stiff DAEs solver.

For slender flexible continua with extreme aspect ratios, the geometric non-linear effects become non-negligible, and traditional small-deformation Euler-Bernoulli beam theory is no longer applicable. This study adopts Geometrically Exact Beam Theory [10,11] to describe the 3D spatial deformation of the sucker rod string.

Geometrically exact beam theory handles arbitrarily large spatial rigid-body rotations and translational displacements without assumptions, and its internal force calculation is entirely based on the current configuration after deformation. The centerline position of the rod cross-section is described by vector $\mathbf{x}(s,t)$, and the cross-section orientation is defined by the orthogonal tensor $\mathbf{R}(s,t) \in SO(3)$. In the local reference frame, the objective generalized 1D strain $\boldsymbol{\varepsilon}$ and curvature $\boldsymbol{\kappa}$ are defined as:

$$\boldsymbol{\varepsilon}(\boldsymbol{s},\boldsymbol{t}) = \boldsymbol{R}^{\boldsymbol{T}}(\boldsymbol{s},\boldsymbol{t})\boldsymbol{x}'(\boldsymbol{s},\boldsymbol{t}) - \boldsymbol{e_1}, \tag{11}$$

$$\boldsymbol{\kappa}(\boldsymbol{s},\boldsymbol{t}) = \mathbf{ax}\left(\boldsymbol{R}^{\boldsymbol{T}}(\boldsymbol{s},\boldsymbol{t})\boldsymbol{R}'(\boldsymbol{s},\boldsymbol{t})\right), \tag{12}$$

where $\mathbf{e_1}$ is the unit direction vector along the beam axis in the undeformed configuration, and $ax(\cdot)$ is the operator extracting the axis vector corresponding to a skew-symmetric tensor.

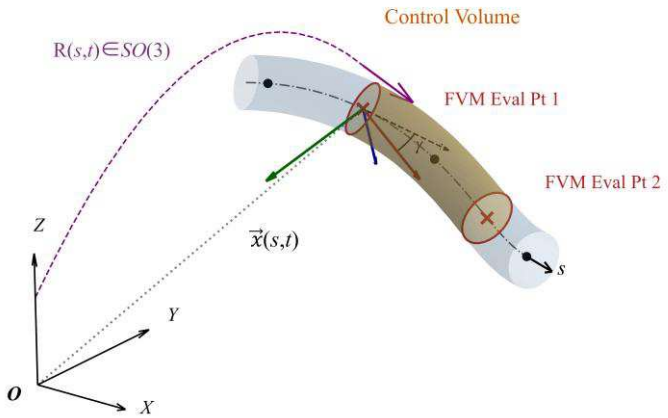


Fig. 2. Kinematic representation and FVM-based discretization of the rod string. The implementation of Geometrically Exact Beam Theory captures finite 3D rotations and shear deformations γ through the rotation tensor $\boldsymbol{R}(s,t)$, while the Finite Volume Method ensures

momentum conservation within the control volume to accurately resolve high-frequency stress wave transients.

For spatial discretization, instead of the traditional weak-form Galerkin method, this study employs the Finite Volume Method based on a three-node beam element architecture. This discretization strategy evaluates the sectional internal forces and moments at two specific Gauss points, establishing a control volume that enforces the conservation of momentum and angular momentum at the element level [25]. This approach effectively suppresses the high-frequency numerical dispersion commonly encountered in traditional finite element methods during transient wave propagation.

Mapping the physical arc-length onto a dimensionless parametric domain $\xi \in [-1,1]$, the generic kinematic field variable $\mathbf{p}(\xi)$ of the continuum is interpolated using parabolic shape functions $\boldsymbol{N_i(\xi)}$:

$$\boldsymbol{p(\xi) = \sum_{i=1}^{3} N_i(\xi)\left(x_i + R_i \tilde{f}_\iota\right),} \tag{13}$$

where $\boldsymbol{N_1 = \frac{1}{2}\xi(\xi - 1), N_2 = 1 - \xi^2}$, and $\boldsymbol{N_3 = \frac{1}{2}\xi(\xi + 1)}$. $\boldsymbol{x_i}$ and $\boldsymbol{R_i}$ are the absolute position and orientation of the i-th structural node, respectively, and $\tilde{\boldsymbol{f}}_\iota$ is the generic offset in the local frame.

Based on the shape functions, the discrete generalized strain vector $\boldsymbol{\varepsilon_k}$ at the k-th evaluation point $\boldsymbol{\xi_k}$ can be explicitly formulated by differentiating the interpolated position field:

$$\boldsymbol{\varepsilon_k = R^T(\xi_k) \sum_{i=1}^{3} N_i'(\xi_k)\left(x_i + R_i \tilde{f}_\iota\right) - \tilde{p}',} \tag{14}$$

where $\tilde{\boldsymbol{p}}'$ represents the initial reference derivative.

For sucker rod systems, damping effects influence transient vibration attenuation and load transmission [6]. In the present work, internal viscoelastic dissipation is modeled using Kelvin–Voigt formulation [26,27]. To accurately simulate the mechanical energy dissipation of high-strength steel during stress wave propagation and suppress non-physical numerical oscillations of stiff Differential-Algebraic Equations under high-frequency excitations, a stiffness-proportional damping term proportional $\mathbf{C} = \beta\mathbf{K}$ to the section stiffness is introduced where the damping coefficient is set to $\beta = 0.01$ in this study.

Consequently, the virtual work $\boldsymbol{\delta\mathcal{L}_{\text{beam}}}$ contributed by the elastic and viscous internal forces over the beam element is formulated as:

$$\boldsymbol{\delta\mathcal{L}_{\text{beam}} = \sum_{k=1}^{2} w_k\left(\delta\varepsilon_k^T F_k + \delta\kappa_k^T M_k\right),} \tag{15}$$

$$\begin{Bmatrix} \mathbf{F_k} \\ \mathbf{M_k} \end{Bmatrix} = \mathbf{K}\begin{Bmatrix} \varepsilon_k \\ \kappa_k \end{Bmatrix} + \beta\mathbf{K}\begin{Bmatrix} \dot{\varepsilon}_k \\ \dot{\kappa}_k \end{Bmatrix} \quad (16)$$

where w_k denotes the quadrature weight. This viscoelastic formulation inherently mitigates high-frequency parasitic oscillations while preserving the fidelity of low-frequency macroscopic stress wave propagation, facilitating robust convergence of the global Jacobian matrix in the DAE solver.

3.2 Distributed fluid loading model

To accurately characterize the elastodynamics of the slender continuum submerged in a viscous fluid, a distributed analytical fluid-structure interaction mechanism is integrated into the GEBT framework. Conventional 1D models frequently lump the fluid inertia into an effective structural density. However, this simplification artificially alters the longitudinal wave speed and misrepresents the viscoelastic energy dissipation within the continuum. To account for the inertia contribution of the surrounding fluid while maintaining the dynamic characteristics of transient stress waves, the added-mass effect is introduced as a distributed acceleration-dependent force rather than being directly incorporated into the structural mass matrix:

$$f_{added,i} = -C_m \rho_f A_r (\ddot{x}_\iota \cdot e_{3i}) e_{3i}, \quad (17)$$

where C_m is the added mass coefficient, ρ_f is the fluid density, A_r is the cross-sectional area of the rod, $\ddot{z}$ is the local axial acceleration, and $\boldsymbol{e_{3i}}$ is the local axial unit vector of the i-th node.

Furthermore, the transverse approach of the rod toward the tubing inner wall is resisted by the squeeze-film effect. Based on the infinitely long journal bearing approximation of the Reynolds equation, the highly nonlinear squeeze-film damping force F_{sq} is theoretically inversely proportional to $(1-\xi^2)^{3/2}$, where ξ is the dimensionless eccentricity ratio. However, direct implementation of this classical formula inevitably triggers catastrophic Jacobian matrix singularities when the rod closely approaches the tubing wall ($\xi \to 1$). Additionally, the activation of the squeeze-film force is unidirectional (only resisting the approaching motion), which introduces a C^0 discontinuity that hinders the convergence of Newton-Raphson iterations.

To systematically circumvent these mathematical bottlenecks, a singularity-free regularized squeeze-film formulation is proposed. A minimal geometric protection factor h_{min}^2 is introduced into the denominator, and a smooth half-wave rectification utilizing the hyperbolic tangent function is employed to continuously filter the radial approach velocity v_r:

$$F_{sq}(\xi, v_r) = \frac{12\pi\mu_f \Delta L R^3}{C_r^3} \frac{\widetilde{v_r}}{\left[(1-\xi^2)^2 + h_{min}^2\right]^{3/4}}, \tag{18}$$

$$\widetilde{v_r} = \frac{1}{2} v_r \left[1 + \tanh\left(K_{reg} v_r\right)\right], \tag{19}$$

where μ_f is the dynamic viscosity, ΔL is the element length, R is the rod radius,C_r is the radial clearance, and K_{reg} regulates the steepness of the velocity transition. This mathematically smoothed formulation ensures that the exact tangent stiffness contribution to the Jacobian matrix remains bounded over the entire configuration space.

According to the principle of virtual work utilized in the multibody solver, these state-dependent analytical fluid forces are mathematically abstracted as absolute forces applied to the structural nodes. The virtual work contribution $\delta\mathcal{L}_{fluid}$ is formulated as:

$$\delta\mathcal{L}_{fluid} = \sum_{i=1}^{N} \delta x_i^T \left(f_{added,i} + f_{sq,i}(x_i, \dot{x}_i)\right). \tag{20}$$

The fluid-inertial and squeeze-film damping terms are assembled into the multibody residual equations as state-dependent nodal forces. This treatment provides a computationally convenient representation of the selected fluid-loading mechanisms within the transient structural model. Because the fluid field and multiphase distribution are not solved explicitly, the formulation should be interpreted as an effective fluid-load model rather than a fully resolved multiphase fluid–structure interaction simulation.

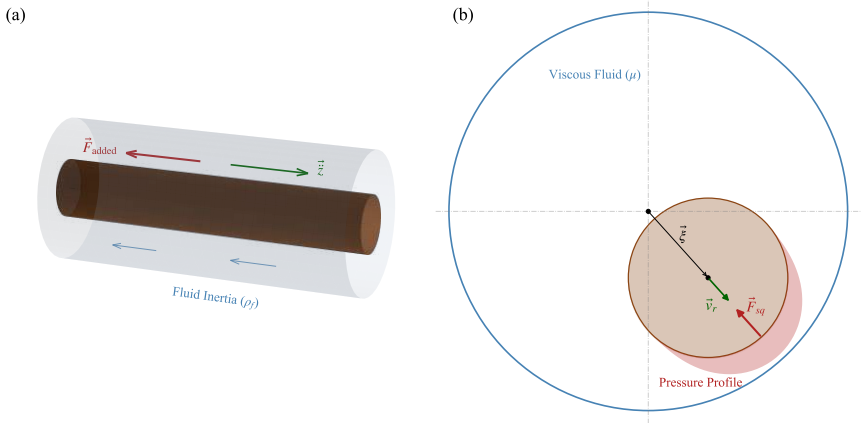


Fig. 3. Schematic representation of the distributed analytical fluid-structure interaction mechanisms. (a) Axial added mass effect, where the acceleration of the rod induces a resisting fluid inertial force. (b) Radial squeeze-film effect based on the Reynolds lubrication theory, illustrating the hydrodynamic pressure profile generation and the resulting damping force opposing the radial approach velocity under a dimensionless eccentricity.

3.3 Rod-tubing contact and friction model

In 3D directional wells, complex wellbore trajectory curvature, transverse gravity components, and rod vibration induced by axial high pressure collectively lead to frequent impacts and

severe friction between the sucker rod and the tubing [28]. To accurately resolve this highly nonlinear boundary condition without incurring the exorbitant computational cost of 3D mesh-to-mesh collision detection, a dimension-reduction contact strategy is adopted [29]. The spatial trajectory of the wellbore is entirely encoded into the distribution of local transverse loads. Consequently, the 3D contact problem is projected onto a 2D local cross-sectional plane, where the radial penetration is continuously evaluated based on the geometric clearance.

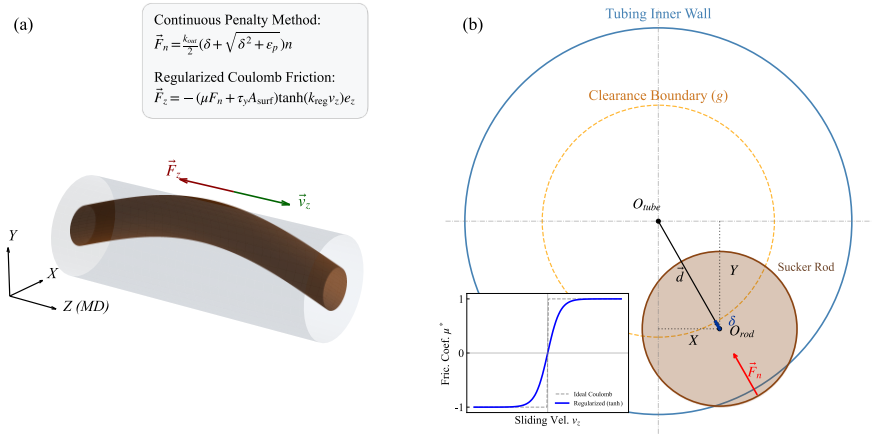


Fig. 4. Schematic of the 3D non-linear rod-tubing contact model and numerical regularization mechanism. (a) Spatiotemporal interaction between the bent rod and tubing, defining the axial sliding velocity $\mathbf{v}_z$ and the opposing friction force $\mathbf{F}_z$. (b) Micromechanical description of the eccentric contact within a 2D cross-section, where the radial penetration depth δ is quantified by the eccentricity vector $\mathbf{d}$ and clearance boundary g.

Within the MBDyn framework, the rod-tubing interaction is mathematically modeled utilizing the deformable displacement joint. Consider the interaction between the dynamic rod node and the static tubing geometry. The instantaneous 3D relative position vector $\boldsymbol{d}$ and relative velocity $\dot{\boldsymbol{d}}$ evaluated at the contact interface are defined as:

$$d = x_2 + f_2 - x_1 - f_1, \tag{21}$$

$$\dot{d} = \dot{x_2} + \omega_2 \times f_2 - \dot{x_1} - \omega_1 \times f_1, \tag{22}$$

where $\boldsymbol{f_1}$ and $\boldsymbol{f_2}$ are the local geometric offsets accommodating the respective radii of the tubing and the rod couplings. A consistent linearization of the generalized contact forces $\tilde{\mathbf{F}}(\tilde{\mathbf{d}}, \dot{\tilde{\boldsymbol{d}}})$ is included in the tangent Jacobian to improve the convergence behaviour of the nonlinear iterations during contact activation and impact events.:

$$\delta \boldsymbol{F_i} = (-1)^i \boldsymbol{R_{1h}} \left(\frac{\partial \tilde{\boldsymbol{F}}}{\partial \tilde{\boldsymbol{d}}} \delta \tilde{\boldsymbol{d}} + \frac{\partial \tilde{\boldsymbol{F}}}{\partial \dot{\tilde{\boldsymbol{d}}}} \delta \dot{\tilde{\boldsymbol{d}}} \right) - \boldsymbol{F_i} \times \boldsymbol{\theta_{1\delta}}. \tag{23}$$

For each discrete node, the instantaneous relative displacement vector in the transverse plane is denoted as $\widetilde{\mathbf{d}_\perp}=[\widetilde{d_x}, \widetilde{d_y}]^{\mathrm{T}}$. The effective radial offset Δr is calculated as:

$$\Delta r = \sqrt{\widetilde{d_x^2} + \widetilde{d_y^2} + \epsilon_0}, \tag{24}$$

where ϵ_0 is an infinitesimally small parameter introduced to eliminate the non-differentiability singularity at the origin ($\Delta r \to 0$) during the Jacobian matrix assembly.

To ensure the C^1 continuity of the Jacobian matrix during Newton-Raphson iterations, a smoothed continuous penalty formulation is implemented to evaluate the normal contact force F_n:

$$F_n = \frac{K_c}{2}\left[(\Delta r - g_c) + \sqrt{(\Delta r - g_c)^2 + \epsilon_p}\right], \tag{25}$$

where K_c is the equivalent contact stiffness, g_c represents the local radial clearance accounting for the geometry of the rod couplings, and ϵ_p is a minimal geometric smoothing factor. The regularized penalty formulation keeps the contact-force transition continuous and helps maintain a bounded tangent contribution during the implicit solution procedure.

Simultaneously, the axial resistance F_z along the wellbore direction comprises the Coulomb friction generated by the rod-tubing contact and the viscous yield resistance of the fluid. Because the classical Coulomb friction model exhibits mathematical discontinuities at the velocity stagnation point ($\dot{\tilde{d}}_z = 0$), a regularization technique is employed [30]. The total axial resistive force is mapped through a hyperbolic tangent function:

$$F_z = -\left(\mu F_n + F_{yield}\right)\tanh\left(K_{reg}\dot{\tilde{d}}_z\right), \tag{26}$$

where μ is the friction coefficient, F_{yield} is the resistance induced by the fluid yield stress over the nodal control volume.

Ultimately, based on the principle of virtual work utilized by the deformable displacement joint, the generalized contact force vector $\mathbf{F}_{contact} = \left[F_n\frac{\widetilde{d_x}}{\Delta r}, F_n\frac{\widetilde{d_y}}{\Delta r}, F_z\right]^T$ is distributed to the system equilibrium equations. The virtual work contribution $\delta\boldsymbol{\mathcal{L}}_{contact}$ is explicitly defined in the local reference frame as:

$$\delta\boldsymbol{\mathcal{L}}_{contact} = \delta\widetilde{\boldsymbol{d}}^T\mathbf{F}_{contact}\left(\tilde{d}, \dot{\tilde{d}}\right), \tag{27}$$

This integrated contact-friction model resolves the multi-axial dynamic coupling induced by the 3D confinement.

Furthermore, a discrete mapping strategy is established to project the global wellbore trajectory into nodal load distributions. To ensure the C^2 continuity of spatial curvature across the entire well section, the 3D survey dataset is interpolated utilizing cubic splines [22]. The effective

distributed load, comprising gravity and fluid buoyancy, is decomposed into the local cross-sectional reference frame of the tubing. Defined by the instantaneous inclination angle ϕ and azimuth angle θ, the equivalent lateral gravity components per unit length, $\mathrm{f}_{\mathrm{lat}} = \left[f_{\mathrm{gx}}, f_{\mathrm{gy}}\right]^T$, are formulated as:

$$\begin{cases} f_{\mathrm{gx}} = (m - \rho_f A_r)\, g \sin\phi \sin\theta \\ f_{\mathrm{gy}} = (m - \rho_f A_r)\, g \sin\phi \cos\theta \end{cases}, \tag{28}$$

where m is the mass per unit length. Consequently, the rod-tubing contact problem is mathematically reduced to a radial offset search within the 2D local plane, effectively encoding the 3D wellbore trajectory into the transverse load manifold.

Importantly, this dimensionality reduction is exclusively confined to the local geometric clearance detection to mitigate the exorbitant computational overhead of 3D mesh-to-mesh collision algorithms. The global structural dynamics, encompassing 3D large-scale bending and torsion, remain governed by the spatial GEBT framework. This formulation provides the contact forces and relative velocities required to evaluate frictional work along the modeled rod string while retaining the three-dimensional structural description.

3.4 Pump and valve model

The transient evolution of the downhole pump load acts as the primary excitation source for the rod string dynamics. Accurately modeling the non-linear reversal process—from downstroke unloading to upstroke loading—presents a severe computational challenge. An instantaneous step load can excite non-physical high-frequency components and deteriorate the conditioning of the nonlinear system, particularly when the spatial discretization is required to resolve transient stress-wave propagation.

To seamlessly integrate this boundary condition within the monolithic DAE solver, an internal state-space formulation is proposed. A dimensionless internal state variable $y \in (0,1]$ is introduced to characterize the effective opening of the pump valve.

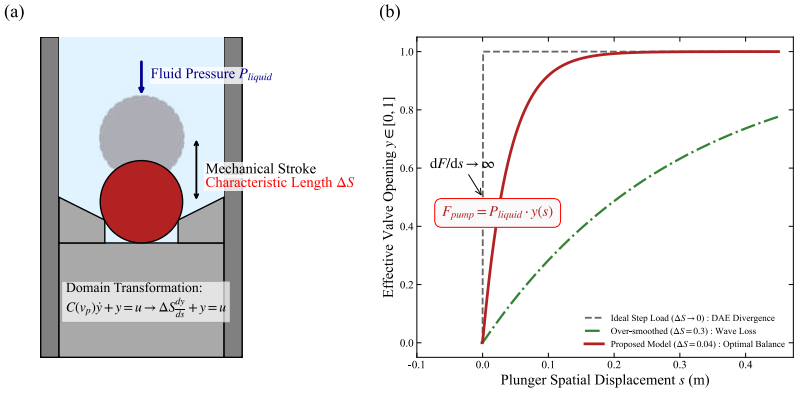


Fig. 5. Physical mechanism and spatial regularization of pump valve loading. (a) Theoretical mapping of the valve dynamics from the temporal to the spatial displacement domain via the characteristic relaxation length ΔS. (b) Numerical sensitivity of valve opening profiles.

The dynamic evolution of the pump valve opening y is governed by the following first-order non-linear differential equation:

$$\frac{|\dot{x_n}|+\epsilon}{\Delta S}\dot{y} + y = \frac{1}{2}\left[1 + \tanh\left(K_{reg}\dot{x_n}\right)\right], \tag{29}$$

where $\dot{x_n}$ is the instantaneous axial velocity of the plunger node. Crucially, ΔS denotes the characteristic spatial relaxation length. According to the chain rule, the state-dependent time constant $\tau_y = \Delta S/(|\dot{x_n}| + \epsilon)$ mathematically maps the temporal discontinuity into a finite spatial transition, providing a loading profile compatible with the resolution limits of the spatial discretization.

Here, ΔS is defined as the characteristic relaxation length, physically corresponds to the mechanical stroke of the traveling valve ball seating and the localized compressibility of the fluid in the pump. From a computational perspective, an instantaneous step load constitutes a primary source of high-frequency numerical dispersion and potential Jacobian singularities in a discretized rod string model.

Sensitivity analysis indicates the low-pass filtering effect of this parameter in the frequency domain: if $\Delta S \to 0$, the load gradient $\partial F/\partial t$ tends to infinity, which not only excites non-physical high-frequency spurious modes of the slender sucker rod string, but also causes the condition number of the MBDyn Jacobian matrix to deteriorate sharply, causing Newton-Raphson iterations to diverge due to the inability to handle rigid impacts. If choose a larger ΔS, the hysteresis effect of the equation becomes too strong, making the loading slope of the dynamometer card over-smoothed and artificially erasing the physical impact characteristics of stress waves on the rod string.

As described in the theoretical treatment of absolute forces with internal states, the transient liquid column load applied to the downhole structural node is formulated as $F_{pump}(t) = P_{liq} \cdot y(t)$, where P_{liq} is the total static load of the liquid column. To ensure rigorous algorithmic stability during the implicit time integration, the analytical perturbations of both the applied force and the internal state are assembled into the coupled system Jacobian matrix:

$$\delta F_{pump} = P_{liq}\delta y, \tag{30}$$

$$\delta \dot{y} = \mathcal{J}_y \delta y + \mathcal{J}_{\dot{x}} \delta \dot{x}_n, \tag{31}$$

where the Jacobian submatrices $\mathcal{J}_y = \delta \dot{y}/\delta y$ and $\mathcal{J}_{\dot{x}} = \delta \dot{y}/\delta \dot{x}_n$ represent the exact linearization of the non-smooth governing equation. This monolithic coupling maintains C^1 continuity in the global DAEs, effectively mitigating numerical chattering at the load onset while retaining a sufficiently steep wavefront to capture the true transient stress wave propagation.

3.5 Electromechanical driving boundary model

In conventional pumping-unit simulations, the surface drive is often represented by prescribed crank kinematics or a simplified prime-mover model. Gibbs noted in his foundational work that if fluctuations in the prime mover speed are neglected, the crank angular velocity may be regarded as constant [31], a simplification widely adopted in subsequent numerical studies. However, initial sensitivity tests conducted in this study regarding spatial discretization revealed a critical conflict in computational mechanics: when high-resolution spatial scales are employed, high-order modes of the slender rod string are significantly excited. In this context, absolutely rigid kinematic boundaries are mathematically equivalent to infinite mechanical impedance [32], failing to yield to high-frequency collision stress waves transmitted from downhole. This non-physical rigid constraint was observed to produce stronger high-frequency oscillations and poorer nonlinear convergence in the refined-mesh benchmark.

To evaluate the numerical robustness of the electromechanical boundary under high-resolution discretization, a separate benchmark case with a refined mesh was analyzed. The results indicate that the conventional rigid kinematic boundary, when subjected to this refined discretization, fails to sufficiently dissipate high-frequency stress waves, eventually triggering numerical chattering and Jacobian ill-conditioning. Conversely, the introduced passive electromechanical boundary successfully attenuates the impacts via electromagnetic impedance matching. This approach not only restores the integrity of the dynamic manifolds but also substantially reduced the number of nonlinear iterations in the refined-mesh benchmark.

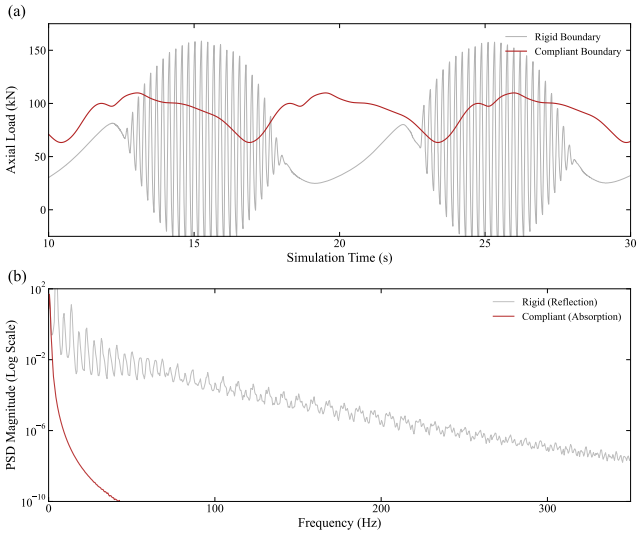


Fig. 6. Comparative analysis of the transient axial load under rigid and compliant boundaries. (a) time-domain profiles; (b) power spectral density (PSD) magnitude. The comparison demonstrates that the compliant electromechanical boundary provides the dynamic flexibility to buffer high-frequency transients.

In this study, a reduced-order equivalent DC-motor model is introduced to provide finite electromechanical compliance at the crank boundary. The model is used to examine the influence of drive-boundary compliance on transient rod-string dynamics and stress-wave transmission. It is not intended to reproduce the detailed electromagnetic behavior of the field induction motor or the internal control architecture of an installed variable-frequency drive. This model incorporates the electromagnetic conversion mechanism into the right-hand side of the multibody system, with its dynamic behavior governed by the following ordinary differential equations:

$$\begin{cases} V_{in} = \mathrm{L}\dfrac{di}{dt} + \mathrm{R}i + \mathrm{G}\omega \\ \tau_{em} = G \cdot i \end{cases}, \tag{32}$$

where V_{in} denotes the input voltage; L and R represent the stator inductance and internal resistance, respectively; G is the electromechanical torque constant; ω is the instantaneous mechanical angular velocity of the crankshaft; and τ_{em} is the output electromagnetic torque.

To elucidate the algorithmic origin of this dynamic impedance matching, the monolithic coupling between the structural rotational degrees of freedom and the electrical internal states must be evaluated at the Jacobian matrix level. Within the MBDyn DAE framework, the virtual perturbation of the electromechanical coupled system yields:

$$\delta\tau_{em} = G\delta i, \tag{33}$$

$$L\delta i + R\delta i + G\delta\omega = \delta V_{in}, \tag{34}$$

Utilizing an implicit time integration scheme where the derivative perturbation is proportional to the state perturbation (i.e., $\delta i = c \cdot \delta i$, being a method-specific integration coefficient), the

coupled sub-matrix contributed to the global tangent Jacobian takes the following skew-symmetric-like form:

$$\begin{bmatrix} \mathbf{J}_{ww} & -G\mathbf{e}_{axis} \\ G\mathbf{e}_{axis}^{T} & Lc + R \end{bmatrix} \begin{bmatrix} \delta\omega \\ \delta i \end{bmatrix} = \begin{bmatrix} \mathbf{0} \\ \delta V_{in} \end{bmatrix}, \tag{35}$$

where $\mathbf{J}_{ww}$ is the structural tangent stiffness/damping block, and $\mathbf{e}_{axis}$ is the unit vector of the rotational axis.

The off-diagonal terms in the coupled electromechanical equations link the crank angular velocity to the electrical current. Together with the electrical resistance and the imposed voltage boundary, this coupling introduces finite dynamic impedance at the drive boundary and permits energy exchange between the electrical and mechanical subsystems. When the system encounters downhole impact loads, the dynamic equations of the motor allow for transient fluctuations in the rotational speed, converting a portion of the mechanical impact energy into regenerative electrical energy under back-EMF or dissipating it as resistive heat. The resulting effect on transient-wave transmission is evaluated from the simulated response relative to the rigid kinematic boundary.

To examine the interaction between voltage modulation and transient rod-string dynamics, an asynchronous adaptive voltage modulation (AAVM) law with a prescribed start-up profile is introduced. The modulation law adjusts the equivalent input voltage as a function of the modeled suspension-point velocity. The feedback gain is treated as a numerical control parameter used to compare boundary responses under the same well configuration and operating condition. Because the formulation is based on an equivalent DC-motor model and a prescribed voltage law, the resulting AAVM responses should be interpreted as modelled control scenarios rather than as predictions of the performance of a specific field-installed VFD. The governing boundary equation is defined as:

$$V_{in}(t) = \underbrace{V_{nom}(1 - e^{-at})}_{Open-loop\ Soft\ Start} - \underbrace{\Delta V\left(1 - e^{-bt}\right)\tanh(k \cdot v_z(t))}_{Active\ Impedance\ Compensation}, \tag{36}$$

where V_{nom} = 325 V is the base voltage maintained for the rated stroke rate; a and b are the time decay constants for the main and feedback loops, respectively, with $a = 0.15\ \mathrm{s}^{-1}$ and $b = 0.10\ \mathrm{s}^{-1}$ set in this study. The rate of voltage modulation is determined by b. Since the establishment time of the electrical compensation is significantly longer than the inherent physical time-lag of the transient stress waves, the AAVM consistently operates in an asynchronous response state across the spatiotemporal domain. ΔV represents the voltage feedback gain boundary, used to simulate the transient power adjustment behavior of modern variable frequency drives during heavy-load reversals:

$$M\dot{q} - p + \mathbf{\Phi}_{/\mathrm{q}}^{T}\lambda = 0, \tag{37}$$

$$\dot{p} + \left(\boldsymbol{\Phi}_{/\mathrm{q}}\dot{\boldsymbol{q}} + \boldsymbol{\Phi}_{/t}\right)_{/\mathrm{q}}^{\boldsymbol{T}}\boldsymbol{\mu} + \boldsymbol{\Phi}_{/\mathrm{q}}^{\boldsymbol{T}}\dot{\lambda} = F(q, \dot{q}, q_{\tau}, t), \tag{38}$$

$$\boldsymbol{\Phi}(q, t) = 0, \tag{39}$$

where the right-hand side force vector $\boldsymbol{F}$ dynamically encompasses the state-dependent delayed control $F_{drive}\left(t, x_{surf}(\dot{t} - \tau)\right)$.

3.6 Numerical solution

Due to the presence of 3D rod-tubing contact and transient fluid loads, the system stiffness matrix exhibits high nonlinearity and abrupt mutations in the time domain. Preliminary simulations using alternative implicit schemes showed reduced robustness for the present strongly non-smooth problem. Therefore, the Bathe composite integrator was selected.

To balance computational efficiency for large time steps with numerical robustness, this study employs the Bathe composite implicit time integrator to solve the full-system DAEs where asymptotic spectral radius is set to ρ_{∞}=0.6 in this study. The convergence of the implicit Newton-Raphson iterations is controlled with a relative tolerance of 10^{-3} for the residuals. While the maximum iteration limit is conservatively set to 500 to ensure robustness during extremely non-smooth contact transitions, the framework demonstrates superior computational efficiency compared with conventional high-fidelity finite-element-based approaches for full-scale transient analysis. For one minute transient simulation, the GEBT-FVM solver completes the computation in approximately 4 hours on a standard workstation using the Bathe integrator and the UMFPACK linear solver.

In DAE systems involving pre-tension and complex contact topologies, the initial assembly at $t = 0$ represents the most significant challenge for the solver. Direct application of gravity and full liquid column loads often leads to the collapse of Newton-Raphson iterations due to singularities in the residual vector derivatives.

To establish a consistent initial manifold, an adaptive pseudo-time step algorithm (dCoef) is enabled during the initial derivatives phase. The solver begins with a trial value of 1.0×10^{-6}

589 and automatically scales the impedance ratio based on the condition number of the Jacobian
590 matrix, thereby smoothly establishing the initial static equilibrium in the system containing 3D
591 penalty contact forces.
592
593 Additionally, to avoid ill-conditioned Jacobian matrices caused by transient load application, a
594 C^{∞} continuous exponential time masking function $\Gamma(t)$ is introduced across all dynamic
595 driving terms:
596 $$\Gamma(t) = 1 - e^{-\gamma t}, \quad (40)$$
597 where the decay factor γ determines the relaxation time of the transition segment. This
598 physical smoothing strategy forces the system into a zero-excitation state during the initial
599 infinitesimal duration, which not only physically simulates the inductive lag associated with
600 the electrical time constant in a real motor armature circuit, but also mathematically
601 circumvents the non-differentiability of the Heaviside step function at $t = 0$, ensuring the
602 global robustness of the simulation.
603
604 **4. Results and discussion**
605 4.1 Model calibration against field dynamometer data
606 The measured surface dynamometer card is used to calibrate and assess the global load–
607 displacement response of the pumping-unit/rod/pump system [31]. To reduce differences
608 associated with sampling and curve alignment, the measured and simulated cards are compared
609 after geometric envelope alignment, as illustrated in Fig. 7. The resulting error metrics quantify
610 the agreement of the aligned card profiles under the investigated operating condition. The
611 calibration uses the surface dynamometer card and is intended to establish a practical parameter
612 set for the case study. The subsequent depth-dependent contact, stress-wave, and wear results
613 are model predictions assessed against the available field evidence.

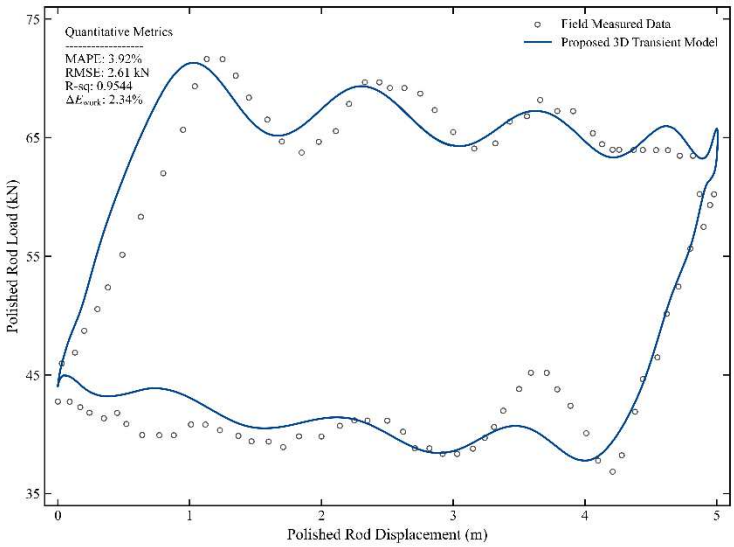


Fig. 7. Calibration result of the proposed 3D transient multibody model against field-measured dynamometer data. The agreement in the global load–displacement loop indicates that the calibrated model reproduces the primary surface dynamic characteristics of the investigated well.

A pure spatial domain geometrical envelope alignment algorithm is proposed in this study. This algorithm first identifies the extreme points of the polished rod displacement to achieve physical separation of the hysteresis loops, and subsequently uses linear interpolation to map the loads onto a standardized 200-point displacement grid. Evaluation results based on the GEAA algorithm demonstrate that the proposed model exhibits high accuracy.

$$Err_{idx}=\frac{|V_{sim}-V_{field}|}{V_{field}}\times 100\%, \tag{41}$$

$$MAPE=\frac{100\%}{n}\sum_{i=1}^{n}\frac{F_{sim,i}-F_{field,i}}{F_{field,i}}, \tag{42}$$

$$RMSE=\sqrt{\frac{1}{n}\sum_{i=1}^{n}(F_{sim,i}-F_{field,i})^2}, \tag{43}$$

$$R^2=1-\frac{\sum_{i=1}^{n}(F_{field,i}-F_{sim,i})^2}{\sum_{i=1}^{n}(F_{field,i}-\bar{F}_{field})^2}. \tag{44}$$

Given the inaccessibility of direct micro-mechanical measurements in the 1.7 km continuum, a systematic multi-objective calibration based on the GEAA was performed to identify the optimal fluid added-mass (C_m) and spatial regularization ($\mathbf{\Delta S}$) parameters (Table 1.).

Table 1. Multi-objective calibration and quantitative error metrics

C_m (-)	ΔS (m)	MAPE (%)	RMSE (kN)	R-sq (-)	ΔE_{work} (%)
2.0	0.01	6.23	4.31	0.8756	6.15
2.0	0.1	3.92	2.61	0.9544	2.34
2.0	0.15	4.04	2.43	0.9603	0.98
1.0	0.1	3.94	2.63	0.9537	2.15
0.5	0.1	4.17	2.89	0.9439	3.10

The calibration results reveal a strong coupling effect inherent to the fluid added-mass coefficient. Altering this parameter simultaneously shifts the global inertial load boundaries and modifies the effective density of the continuum, thereby shifting the phase velocity of the transient stress waves. Consequently, an optimal added-mass coefficient ($C_m = 2.0$) that aligns the high-frequency stress ripples during the upstroke may introduce minor phase discrepancies during the unloading downstroke. This trade-off reflects the limitation of using a spatially constant effective added-mass coefficient to represent the fluid-inertia effects in the investigated well. Variations in local phase distribution and time-dependent multiphase effects are not explicitly resolved by the present formulation.

Furthermore, the spatial regularization length primarily controls the spatial extent of the load transition without modifying the material stiffness of the rod string, while the Kelvin-Voigt proportional damping exhibits excellent orthogonality, dissipating only high-frequency kinematic ringing without distorting the macroscopic hysteresis loop.

Acknowledging the impossibility of achieving absolute local alignment due to the unified, singularity-free mathematical formulation of the DAE boundary, the selected parameter set represents the optimal compromise. It robustly bounds the extreme alternating stress envelopes while improving numerical robustness, satisfying the fundamental prerequisites for the subsequent control-structure interaction and fatigue evaluations.

In terms of curve morphology, the blue simulation curve largely replicates the main evolutionary features of the field data. It can be observed that both the simulation and field-measured curves exhibit significant high-frequency ripples during the upstroke and downstroke plateau phases. The simulated ripples are consistent with stress-wave propagation and reflection within the rod string. Their exact amplitudes should nevertheless be interpreted cautiously because the field measurements have limited sampling bandwidth and the model employs reduced-order fluid and valve representations. In contrast, this study utilizes the Bathe integrator with a time step of $\Delta t = 0.001s$ for time advancement, which not only suppresses numerical dispersion but also allows for the accurate capture of true transient impact responses.

Some discrepancies remain between the simulated and measured dynamometer cards. The present fluid-loading representation uses prescribed effective fluid properties and a reduced pump/valve model; it does not explicitly resolve transient gas–liquid phase distribution, incomplete pump fillage, or phase-dependent damping. Consequently, the high-amplitude oscillations associated with fluid pound in the field measurements are not reproduced explicitly. The card comparison therefore assesses the global load–displacement response for the investigated condition rather than providing a detailed validation of multiphase hydraulic transients.

4.2 Electromechanical drive effects on transient load transmission

The energy transfer between the surface driving system and the downhole flexible rod string is a representative large-lag, strongly coupled nonlinear process. This section provides an in-depth analysis of the electromechanical interaction features during the startup phase and steady-state operation based on the data extracted from MBDyn.

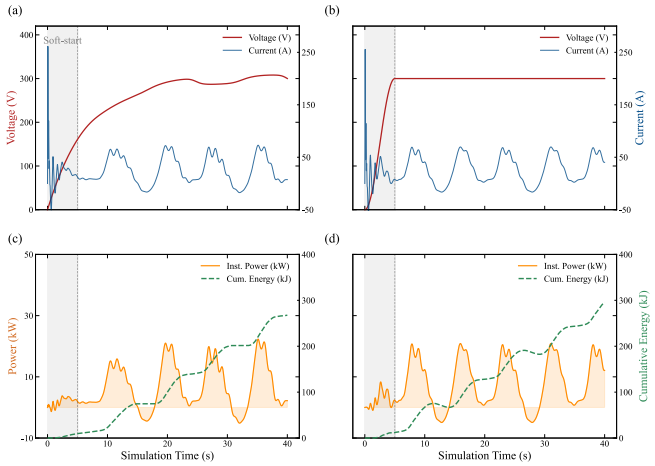


Fig. 8. Transient electromechanical responses and energetic metrics of the modelled constant-voltage and AAVM drive-boundary cases. (a) Prescribed voltage and current responses for the AAVM scenario; (b) responses for the constant-voltage baseline; (c,d) simulated power and cumulative-energy histories under the respective energy-handling assumptions. Shaded regions indicate the prescribed start-up interval.

Observing the 0 – 5 s interval in Figures (a) and (b), a peak startup current of approximately 250 A occurs regardless of the driving mode. This is due to the substantial initial static friction and rotational inertia of the 1707 m tapered rod string. In the early stages of electromagnetic field establishment, the motor has not yet generated sufficient back-EMF, resulting in a rapid surge in current. The imposed soft-start masking function limits the simulated current surge and improves numerical robustness during initialization.

Analysis of the cumulative energy consumption in Figures (c) and (d) shows that within the same steady-state cycle, the AAVM drive exhibits higher cumulative energy consumption compared to the conventional constant voltage drive. This difference stems from the different handling mechanisms for regenerative energy. In the present drive model, negative mechanical power is treated differently in the two cases. The CV case permits regenerative power transfer, whereas the AAVM case assumes dissipation through a braking resistor.

To further investigate the simulated voltage-modulation boundary on the full-well transient dynamic behavior, spatiotemporal evolution curves of the axial load at three critical depths—the excitation source, the transmission path, and the feedback boundary —were plotted based on the computational data, as shown in Figure 9. Comparing the transient responses of the traditional constant voltage drive and the adaptive feedback voltage modulation, Figure 9 reveals two types of multiscale dynamic phenomena that are difficult to capture in traditional single-phase coupling analysis.

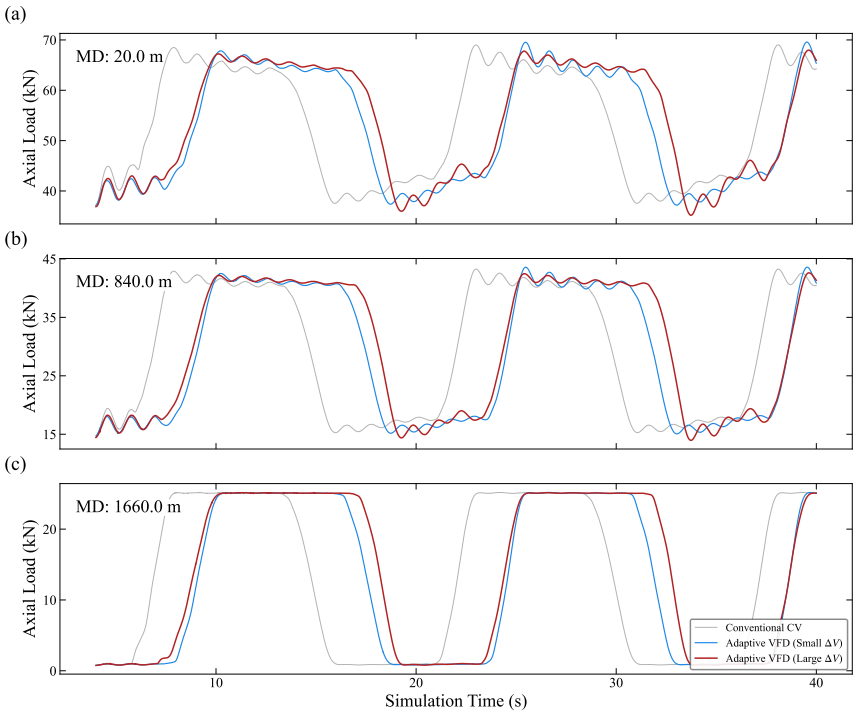


Fig. 9. Spatiotemporal evolution of transient axial loads under different surface driving modes. (a) Surface section (MD 20.0 m); (b) Mid-wellbore section (MD 840.0 m); (c) Downhole section (MD 1660.0 m).

On the macro-kinematic scale, the load curves under AAVM across the entire well exhibit a significant global phase lag on the time axis. Even at the excitation source, the reversal actions have become notably misaligned. The behavior of this phenomenon lies in the voltage-slip coupling effect of the system. Under AAVM mode, the voltage modulation based on velocity feedback forces the motor to continuously generate adaptive electromagnetic slip [32]. The system actively reduces the effective input power during load transients, allowing for a certain

loss in rotational speed in exchange for mitigating impacts. Therefore, this kinematic deceleration effect induced by the flexible surface boundary reshapes the true force boundary and motion rhythm at the well bottom through the force transmission of the extremely long continuum.

On the micro-wave-dynamic scale, the time-domain profiles validate the phase mismatch mechanism of the control-structure interaction. As limited by the finite longitudinal wave propagation speed, the downhole excitations require an inherent physical time-lag of approximately 0.33 s to reach the surface. Consequently, the surface-based active compensation inevitably operates asynchronously with the actual downhole transients. Visually, compared to the conventional CV boundary, the AAVM drives exhibit more intense high-frequency residual ripples, indicating that the delayed feedback inadvertently amplifies the local high-frequency dynamics rather than mitigating them.

However, a multi-scale competition mechanism emerges when comparing the different voltage modulation gains (ΔV). On the macro-kinematic scale, particularly in the peak load regions, the modelled AAVM case (Large ΔV) exhibits a distinct "peak-shaving" effect. The significant voltage drop effectively softens the driving mechanism, resulting in a visible reduction of the macroscopic maximum axial load compared to the CV and Small ΔV cases. This demonstrates a trade-off inherent to the active electrical boundary: a larger feedback gain successfully levels the macroscopic mechanical impedance but simultaneously exacerbates the microscopic high-frequency chattering.

This multiscale dynamic insight reveals a critical limitation: in constrained continua with extreme aspect ratios, surface electrical flexibility is fundamentally bottlenecked by the wave propagation delay. While it can modulate the low-frequency macroscopic loads, it is physically incapable of rapidly dissipating the high-frequency stress waves.

4.3 Stress wave propagation and spatial dynamic response

As a slender elastic structure with a considerable length, the sucker rod string exhibits non-instantaneous load transmission, where surface-induced disturbances propagate along the rod in the form of elastic stress waves [31]. Figure 10 presents the spatiotemporal evolution of the maximum principal stress $\sigma_{max}(s,t)$ during a steady-state operating cycle. Under the joint modulation of tension and localized 3D bending moments, the principal stress is characterized as:

$$\sigma_{max}(s,t) = \frac{F_x(s,t)}{A(s)} + \frac{\sqrt{M_y^2(s,t) + M_z^2(s,t)}}{W(s)}. \tag{45}$$

According to 1D linear elastic wave theory, the propagation of stress waves in the steel rod string is governed by the D'Alembert wave equation.

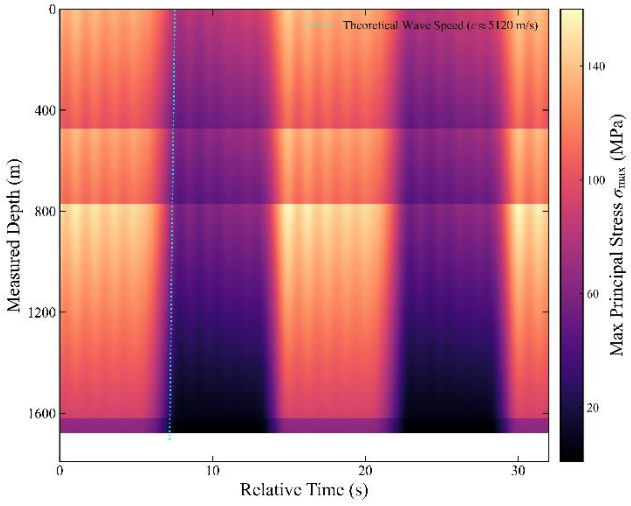


Fig. 10. Spatiotemporal evolution of maximum principal stress along the 1707 m rod string. The simulated wavefront slopes are consistent with the reference longitudinal-wave speed of the steel rod, providing a check on the representation of transient stress-wave propagation at the selected spatial and temporal resolutions.

As shown in Fig. 10, the propagation velocity of the stress wave can be determined by the slope of the high-stress wavefronts in the spatiotemporal domain. This velocity, calculated as the ratio of the spatial travel distance to the temporal duration ($\Delta z_{wave}/\Delta t_{wave}$), is approximately 5110–5130 m/s. This emergent velocity is in excellent agreement with the theoretical longitudinal speed of sound in high-strength steel. It is important to note that the grid ratio defined by the

discretization ($\Delta z_{\mathrm{grid}}/\Delta t_{\mathrm{step}}$=10,000 m/s) is nearly double the physical wave speed. The adopted temporal and spatial resolutions correspond to a nominal Courant number of 0.512. The close agreement between the simulated and theoretical wavefront slopes indicates that the resulting phase error is limited over the propagation distance considered. Furthermore, the rod string exhibits noticeable changes in stress-wave amplitude at depths of 466 m, 767 m, and 1635 m. These variations are associated with mechanical impedance discontinuities caused by changes in rod properties and boundary constraints, resulting in wave reflection and transmission phenomena.

The contour plot shows that at the beginning of the upstroke, around $T = 15s$, a 24.2 kN loading wave generated by the instantaneous closure of the bottom pump valve propagates upward from the well bottom. As this wave passes through the tapered grade transition points, the wavefront undergoes significant splitting and phase delay. The reflected waves and subsequent incident waves undergo coherent superposition in localized areas forming periodic dynamic stress concentration zones. This wave superposition effect results in localized transient peak stresses reaching 140 MPa, far exceeding the static equivalent load calculations. During the middle of the downstroke, after approximately $T = 25s$, although the entire rod string is in a state of relatively low static load, the residual oscillations of the high-frequency stress waves remain clearly visible. These high-frequency stress fluctuations not only increase the alternating stress amplitude σ_a of the material, leading to a risk of fatigue crack initiation, but also significantly enhance the normal impact force F_n at the instant of rod-tubing contact through dynamic load amplification [33].

The distribution of wear energy dissipation reveals intense energy loss in localized well sections, which is essentially related to the spatial instability of the sucker rod string under compression and frequent rod-tubing impacts. This section utilizes the 3D kinematic data extracted from MBDyn to investigate the evolution of the microscopic vibration of the rod string.

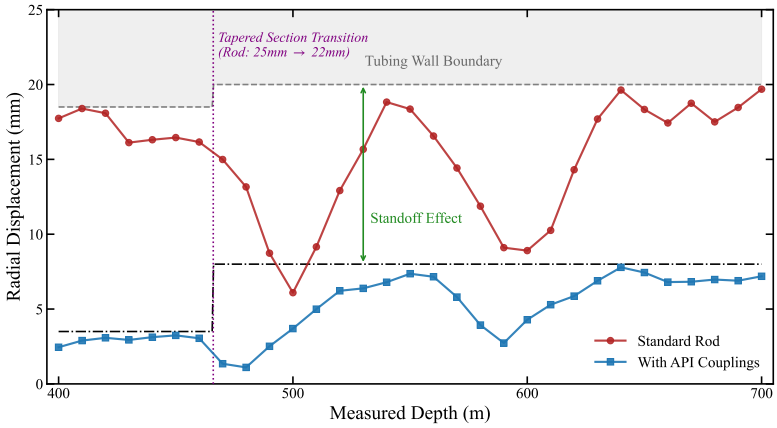


Fig. 11. Comparison of radial displacement profiles for the rod string with and without API couplings. The data demonstrates the standoff effect where discrete coupling constraints preserve radial clearance and mitigate contact between the rod body and the tubing wall.

In deep well dynamic analysis, if the sucker rod is treated as a uniform continuum, the model exhibits significant transverse vibrations induced by stress waves during the middle of the downstroke (Fig. S1). However, this model incorporates the geometric constraints of sucker rod couplings according to API standards. Simulations indicate that for the 1707 m case well, the radial unilateral clearance at the couplings is only 3.5 mm to 6.0 mm. This extremely narrow spatial constraint produces a powerful standoff effect [34]. When the rod string tends toward helical instability due to bottom axial compression, the large-diameter couplings are the first to contact the tubing inner wall, thereby forcing the helical curvature radius to remain locked within a minimal geometric space and effectively mitigating the macroscopic structural instability. This explains the physical fact frequently observed during field rod retrieval, where eccentric wear on the couplings is extremely severe while wear on the rod body is negligible.

To investigate the spatial heterogeneity and the multi-axial dynamic coupling in the physical wellbore, the continuous transient results are extracted from the 3D GEBT-FVM model. Fig. 12 illustrates the axial and cross-dimensional phase trajectories of the rod string at three representative measured depths (MD 0 m, 500 m, and 1700 m) under AAVM control, while

Fig. 13 depicts the corresponding time history and amplitude spectrum of the normal contact force F_n at the same locations.

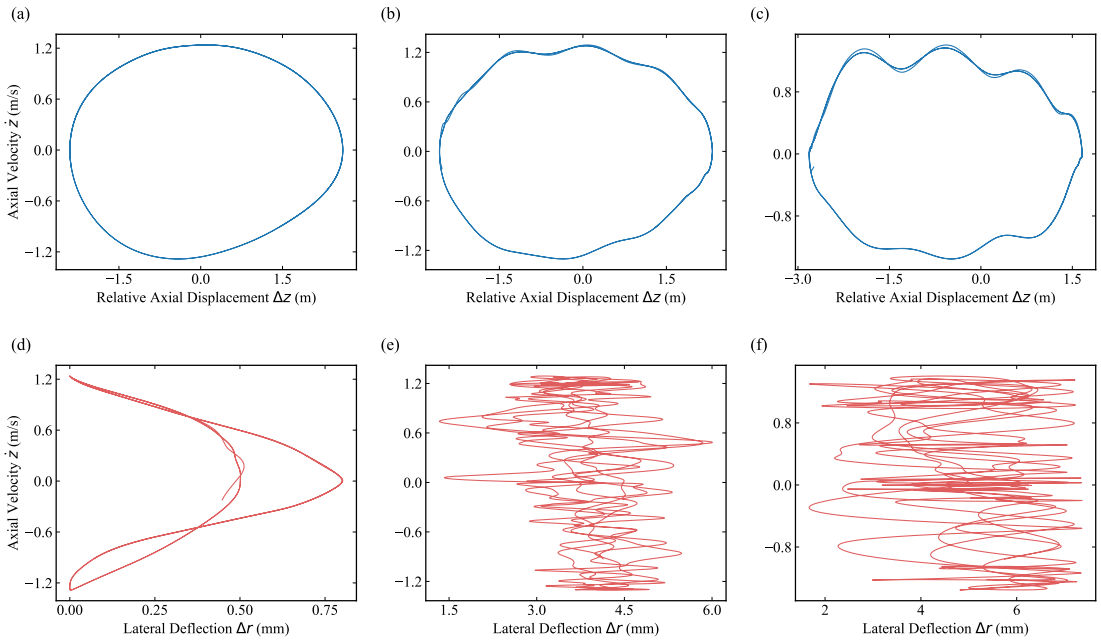


Fig. 12. Transient axial and cross-dimensional phase trajectories at representative measured depths (MD). (a) Axial phase portrait at the surface (MD 0 m); (b) Axial phase portrait at the dogleg section (MD 500 m); (c) Axial phase portrait at the downhole node (MD 1700 m); (d) Cross-dimensional phase portrait at the surface; (e) Cross-dimensional phase portrait at the dogleg section; (f) Cross-dimensional phase portrait downhole showcasing the gravity-induced lateral offset.

The axial phase portraits are presented in Figs. 12(a-c). At the surface node (MD 0 m, Fig. 12a), the trajectory forms a relatively smooth, closed-loop limit cycle with an axial stroke of approximately 5.0 m, which is governed by the kinematic boundaries of the pumping unit. As the stress waves propagate downwards, the phase trajectories undergo progressive geometric distortions. At the dogleg section (MD 500 m, Fig. 12b), high-frequency, low-amplitude ripples emerge along the limit cycle. Upon reaching the downhole node (MD 1700 m, Fig. 12c), these ripples are non-linearly amplified into pronounced multi-frequency fluctuations.

The cross-dimensional phase portraits in Figs. 12(d-f) reveal the multi-axial energy transfer mechanism. At the surface (Fig. 12d), the lateral deflection Δr is constrained within 0.75 mm by the polished rod stuffing box, displaying a symmetrical double-loop pattern. In the dogleg section (Fig. 12e), the rod experiences a substantial lateral deflection ranging from 1.5 mm to 6.0 m. The corresponding contact force F_n (Fig. 13c) remains extremely low, with a maximum value of only $1.2 \times 10^{-3}\ kN$, and the spectrum (Fig. 13d) is dominated by low frequencies below 5 Hz. This implies that owing to the immense axial tension at MD 500m, the strong tension-stiffening effect successfully restrains the lateral deflection within the physical radial clearance. The rod string does not undergo hard wall-impacts in this region; instead, it is stably pulled against the inner wall, resulting in continuous, low-amplitude sliding rubbing.

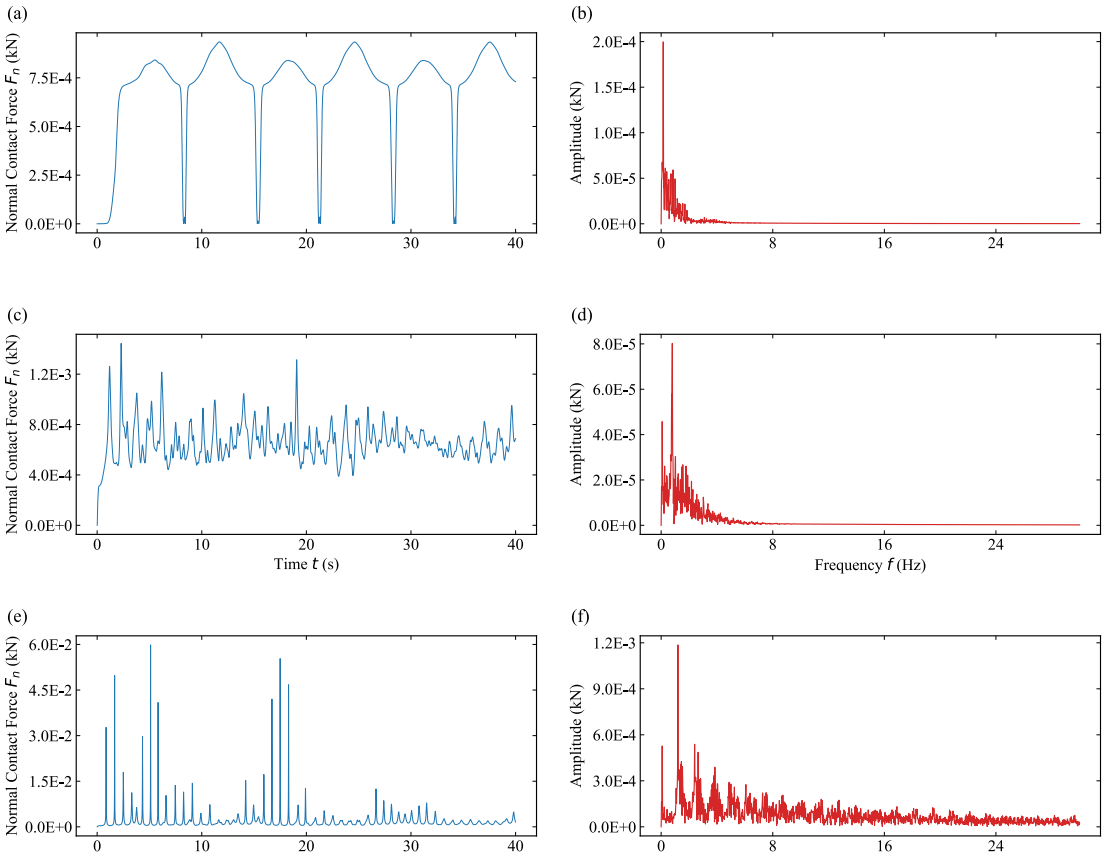


Fig. 13. Time-frequency analysis of normal contact forces at representative measured depths. (a) Time history of the contact force at the surface (MD 0 m); (b) Amplitude spectrum at the surface; (c) Time history of the contact force at the dogleg section (MD 500 m); (d) Amplitude spectrum at the dogleg section; (e) Time history of the contact force at the downhole

node (MD 1700 m) showing coupling-stiffness impacts; (f) Broadband amplitude spectrum downhole.

In the downhole section (MD 1700 m, Fig. 12f), the system dynamics undergo a drastic transition. Due to the accumulation of gravity and inclined wellbore trajectory, the rod string persistently settles near the bottom of the tubing wall, exhibiting a significant lateral offset with Δr shifting to a band of 2.0 mm to 7.0 mm. Unlike the tension-stiffened upper sections, the downhole plunger experiences dynamic axial compression, which triggers non-smooth, intermittent impacts. As plotted in Fig. 13(e), the downhole contact force exhibits sharp impulsive clusters reaching up to $6.0 \times 10^{-2}\ kN$. Consequently, the amplitude spectrum in Fig. 13(f) is heavily populated with dense, broadband chaotic excitations spanning 0 to 25 Hz. This comparative analysis delineates the depth-dependent variations in the rod string's multi-axial dynamic behavior: while the high-tension shallow section exhibits stable, low-amplitude lateral oscillations, the combined effects of downhole compression and gravity-induced offset in the deep section promote non-smooth, high-frequency contact excitation.

4.4 Fatigue integrity assessment and multiscale competition mechanism

Conventional quasi-static models typically assume that the bending response of the rod string remains consistent with the low-frequency periodicity of the macroscopic reciprocating stroke. However, sectional internal force data extracted via the FVM reveal that in well sections with high tension and high dogleg severity, the localized resultant bending moment M_{res} exhibits highly disordered high-frequency oscillation characteristics.

The behavior of this phenomenon lies in the fact that under the action of a massive axial tension F_x, the dynamic behavior of the slender rod string highly regresses into that of a tensioned string structure. Under 3D complex wellbore constraints, any minute rod-tubing impact or fluid disturbance can act as an initial excitation, stimulating transverse modal vibrations containing rich high-order frequency components.

For the present screening-level assessment, the cycle envelope is used to summarize the dominant mean and alternating stress components. In an engineering fatigue screening based on an equivalent stress range and the modified Goodman relation, the key factor determining whether a structure will undergo fatigue fracture is not the transient path of stress in the time domain, but the extreme characteristics of the stress state throughout the load cycle. The width of the envelope in the figure determines the mean tensile stress acting on the rod section, while the height of the envelope defines the maximum alternating bending stress amplitude induced by high-frequency transverse vibrations. Therefore, this study shifts the focus of the dynamic analysis from time-series sequences to the extraction of envelope features in the internal force state space, serving as the physical input for subsequent fatigue limit assessments using the modified Goodman criterion.

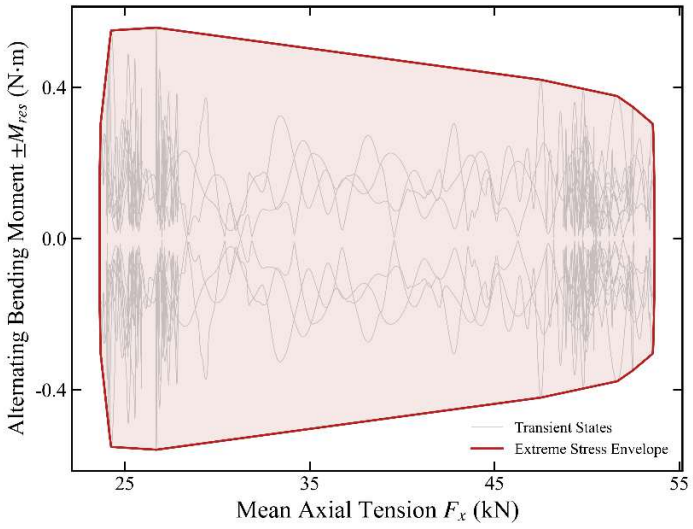


Fig. 14. Extreme stress state envelope for fatigue characterization at MD 470 m. The extracted convex hull captures the non-linear coupling between mean axial tension and high-frequency alternating bending moments induced by lateral vibrations.

Sucker rod fracture is generally associated with fatigue under cyclic axial and bending stresses. This section performs a quantitative integrity assessment of the system based on the nonlinear internal forces extracted across the entire well by MBDyn, combined with the modified Goodman criterion.

Fig. 15(a) presents the distribution of various depth nodes in the space of mean stress σ_m and alternating stress amplitude σ_a within a steady-state cycle. A prominent feature is that the data points are not randomly distributed but exhibit stress clusters corresponding to the five-stage tapered grade transitions. Among these, the first four stages are clearly distinguishable in the figure; the fifth stage, corresponding to the lowermost support rod string, is extremely short at only 26 m, and its points in the stress space are closely connected to the fourth stage, appearing as the shortest blue line segment in the plot.

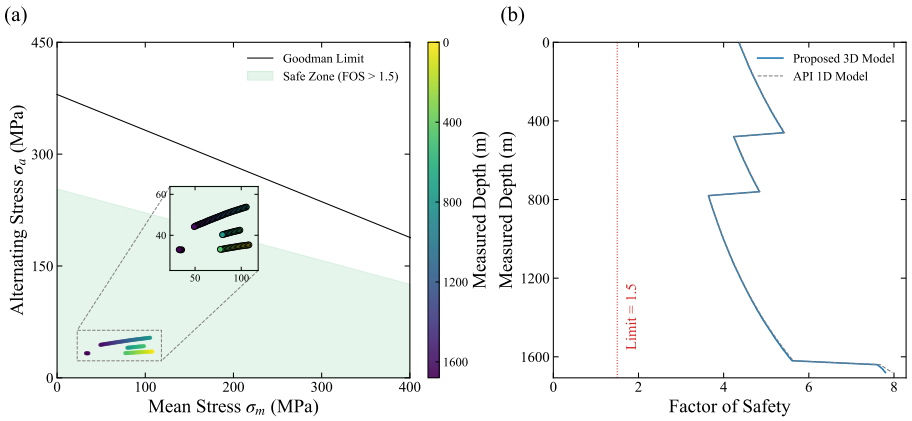


Fig. 15. Fatigue integrity and safety factor profiling of the 1707 m rod string. (a) Distribution of steady-state stress cycles on the Modified Goodman diagram. The stress clusters reflect the loading conditions of different rod segments relative to the material fatigue limit. (b) Comparison of the Factor of Safety predicted by the API 1D model and the proposed 3D transient model along the measured depth. The reference threshold adopted in this study is indicated by the dashed line for reference.

At the grade transition boundaries, the abrupt reduction in cross-sectional area leads to significant jumps in sectional stress under the same axial force. This phenomenon validates the capability of the proposed model to accurately capture stress concentration features induced by geometric discontinuities, providing an accurate load benchmark for refined life prediction.

Figure 15.b presents the evolution curve of the fatigue safety factor with depth across the entire well, comparing the predictions of the traditional API 1D model with the proposed 3D model.

In the tension-dominated sections of the investigated well, the one-dimensional and three-dimensional estimates are similar. In the deeper sections with compression or lower axial tension, the three-dimensional model captures an additional contribution from bending stresses associated with transverse motion and rod–tubing interaction.

However, as the depth increases into the compression zone below 1600 m, the prediction curve of the 3D model begins to shift to the left, indicating a decrease in predicted safety. Although this shift is not prominent in the current case well, it reveals a critical mechanical trend: in the bottom compression or low-tension sections, the contribution of additional bending stresses generated by transverse vibrations excited by stress waves to fatigue damage begins to emerge.

Calculations show that under the constant voltage (CV) baseline, the average safety factors across the entire well are 4.83 (1D) and 4.82 (3D). However, when the AAVM strategy is implemented, the safety factor exhibits a profound non-monotonic evolution dependent on the voltage modulation gain (ΔV), as detailed in Table 2. For low to moderate gains ($\Delta V = 1$ to 30V), the 3D safety factor decreases to 4.78–4.79, underperforming the CV baseline. Conversely, under aggressive the prescribed feedback gain ($\Delta V > 45\ V$), the safety factor progressively recovers and ultimately surpasses the baseline, reaching 4.84 at. $\Delta V = 100$ V.

Table 2. Average fatigue safety factors of the rod string under various driving modes

Driving Mode	**Modulation Gain ΔV (V)**	**Average SF (1D)**	**Average SF (3D)**
CV	-	4.83	4.82
AAVM	1	4.79	4.78
	30	4.81	4.79
	45	4.83	4.82
	60	4.84	4.83
	100	4.85	4.84

This phenomenon fundamentally originates from a multiscale competition mechanism governed by the Modified Goodman criterion. The implementation of active control inherently excites high-frequency micro-chattering due to the uncompensated wave propagation delay. This micro-scale penalty increases the alternating stress amplitude (σ_a), acting to degrade the safety margin. At low ΔV regimes, this parasitic vibration dominates the fatigue evaluation.

However, as ΔV increases to higher regimes, the drastic transient voltage drop grants the motor substantial macroscopic slip compliance. This powerful "peak-shaving" effect severely reduces the maximum macroscopic tension during the upstroke, thereby substantially lowering the mean tensile stress (σ_m). Given that the 1.7 km rod string is heavily tension-dominated, this macro-scale reduction in σ_m eventually outweighs the micro-scale amplification of σ_a.

Consequently, a qualitative conclusion is established: the anti-fatigue efficacy of surface-based active modulation is highly conditional. Insufficient voltage feedback inadvertently deteriorates system integrity via wave-induced phase mismatches and localized chattering. Only when the modulation gain is sufficiently large can the macroscopic compliance override the micro-dynamic penalties.

Comprehensive assessment indicates that under a steady-state 4.0 strokes per minute operating condition, the minimum safety factors for both the constant voltage drive and the AAVM strategy remain significantly above the engineering threshold of 1.5. This suggests that the current five-stage tapered rod design possesses sufficient safety margins under the complex dynamic environment induced by the 3D wellbore trajectory. In this specific well, the core driver of early pipe failure is tubing wear-through rather than sucker rod fatigue failure, thus highlighting the necessity of the 3D transient wear prediction model established in this paper. Because fatigue safety remains adequate in the investigated case, the subsequent intervention focuses on tubing wear rather than rod-string fatigue.

4.5 Frictional energy dissipation and wear localization

The mechanical energy input from the surface drive and transmitted via stress waves is partially consumed to overcome the viscous resistance of the well fluid, while a portion of the transmitted mechanical energy is dissipated through fluid resistance and rod–tubing friction. The wear volume and RUL are evaluated based on the Archard wear law and geometric equivalent mapping. Within a steady-state stroke cycle T, the effective wear work $W_{wear,i}$ at node i converted into pure friction can be expressed as:

$$W_{wear,i}=\eta \cdot \int_{t_1}^{t_2} \mu \cdot F_n(t) \cdot |v_z(t)|dt. \quad (46)$$

The coefficient η=0.94 was supplied by the field operator and is used as a fixed conversion factor in Eq. (46) to define the effective frictional work used in the wear calculation. It is treated as a prescribed input rather than being identified through calibration against the measured tubing-failure time.

According to the classic Archard wear theory, the volume of metal worn during a single cycle V_{cycle} is proportional to the effective frictional work:

$$V_{cycle} = K_w \cdot \frac{W_{fric,i}}{\mu}. \quad (47)$$

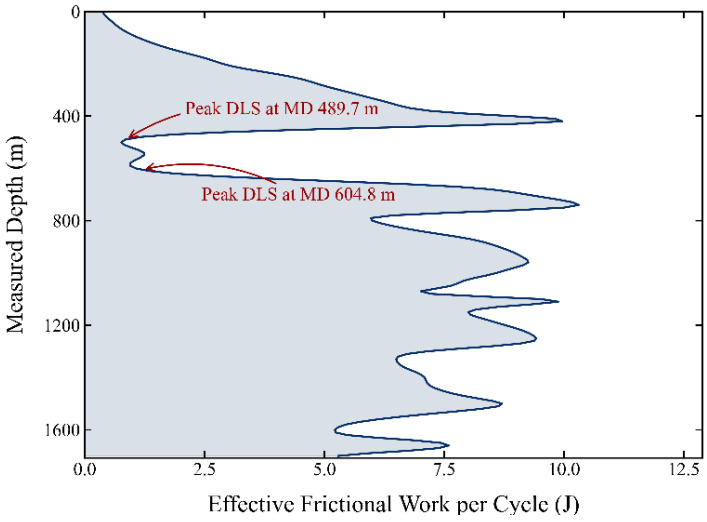
The wear coefficient $K_w = 2.20 \times 10^{-12} m^3/J$ was provided by the field operator for the specified P-110 tubing/high-strength steel sucker-rod contact under water-bearing crude-oil lubrication.

To convert the 3D wear volume dissipation into a 1D radial wear depth h_{cycle}, a geometric mapping approach based on classical sliding wear theory is adopted [35]. The wear volume is assumed to be uniformly distributed over the projected contact area during a single stroke.:

$$h_{cycle} = \zeta K_w \cdot \frac{W_{fric,i}}{\mu \cdot D_{rod} \cdot S_{stroke}}, \quad (48)$$

where D_{rod} is the local rod diameter; Stroke is the true relative sliding distance at the node; and ζ is the material compatibility factor. For rod-tubing contact of identical materials, ζ=1. When centralizers are installed at target nodes, a significant contact stiffness disparity is

993 introduced. Since the hardness of the centralizer is much lower than that of the steel tubing, the
994 vast majority of the surged frictional mechanical energy is absorbed by the softer centralizer in
995 the form of microscopic plastic yielding and shear dissipation during the sliding of dissimilar
996 materials.
997
998 After determining the wear depth per stroke, the onset of tubing perforation is adopted as the
999 physical failure endpoint. At node i, this endpoint is represented by a unilateral wear depth
1000 equal to the local original tubing wall thickness, $t_{wall,i}$. Assuming that the cycle-averaged wear
1001 rate remains constant at the operating condition considered, the remaining time to the through-
1002 wall criterion is estimated as:
1003 $$RUL_i = \frac{0.5 \cdot t_{wall}}{h_{cycle} \cdot N_{year}}, \quad (49)$$
1004 Here h_{cycle} is the estimated unilateral wear depth per stroke cycle, and N_{year} is the average
1005 number of operating cycles per year calculated from the steady-state stroke rate. The resulting
1006 RUL is a model-based estimate for the specified operating condition. Changes in operating
1007 conditions, deposition, corrosion, and time-dependent wear behaviour are not explicitly
1008 represented in this extrapolation.



1009
1010 **Fig. 16. Predicted distribution of effective frictional energy dissipation along the rod**
1011 **string.** The profile reveals significant spatial heterogeneity in wear intensity, where localized
1012 energy peaks at MD 489.7 m and 604.8 m correlate strongly with maximum Dogleg Severity
1013 locations.

The effective wear energy dissipation distribution curve across the entire well provides a quantitative model-based estimate of the spatial variation in wear propensity. The results confirm a significant spatial coupling between peak energy regions and locations of maximum wellbore dogleg severity. Specifically, near MD 489.7 m and MD 604.8 m, the transition in dogleg severity—driven by intense combined changes in inclination and azimuth—directly triggers the nonlinear amplification of the normal contact force F_n. This dynamic response keeps the well section from 600 m to 1100 m in a state of high-intensity lateral squeezing for extended periods, indicating how wellbore curvature promotes localized accumulation of frictional energy.

The predicted high-risk wear peaks show high correlation with the historical maintenance records of the case well: the actual tubing wear-through and leakage point occurred at 1097 m, while the simulation curve exhibits a significant energy aggregation peak near this location. This evaluation metric based on cumulative frictional work, rather than a single lateral force value, better accounts for the cumulative nature of long-distance sliding than an instantaneous contact-force metric under transient dynamic environments. However, to further ascertain the deep mechanical causes behind these high-energy contact points, the 3D instability characteristics of the rod string at specific load phases must be investigated.

4.6 Field corroboration

Macroscopic field inspections serve as the experimental validation for the predicted wear localization. Maintenance records confirmed a severe eccentric wear perforation near the measured depth of 1097 m after 1.25 years of operation. As detailed in Fig. 17, the computed frictional-work distribution shows a high-wear region near this depth. The predicted life of 1.39 years is also close to the recorded service period of 1.25 years. Although this single-well comparison does not constitute a statistical validation, it provides field-based corroboration of the predicted wear localization.

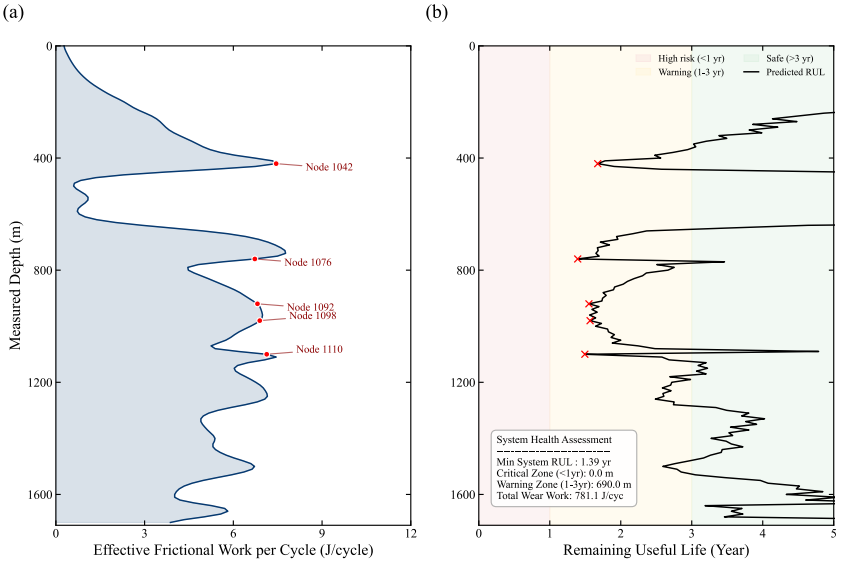


Fig. 17. Depth-dependent profiling of eccentric wear intensity and tubing Remaining Useful Life. (a) Localized peaks in frictional work identify high-intensity contact regions primarily driven by wellbore curvature. (b) The spatial decoupling between minimum RUL and maximum frictional work demonstrates that small-diameter tapered segments exhibit significantly higher vulnerability to service life reduction than thicker sections under equivalent energy dissipation.

The observed failure may also have been affected by factors not explicitly represented in the present model. Field inspection identified organic and inorganic deposits in the tubing. Such deposits can alter the effective clearance and contact conditions, while corrosion and deposition-related changes in the contact surface are not explicitly modeled. The predicted wear distribution should therefore be interpreted as an estimate under the prescribed geometry, fluid properties, and wear relation, rather than as a complete reconstruction of the time-dependent field deterioration process.

4.7 Targeted centralizer placement assessment

Addressing the multiple severe wear points exposed under the baseline condition, this paper proposes a targeted centralizer optimization placement scheme driven by the minima of the remaining useful life.

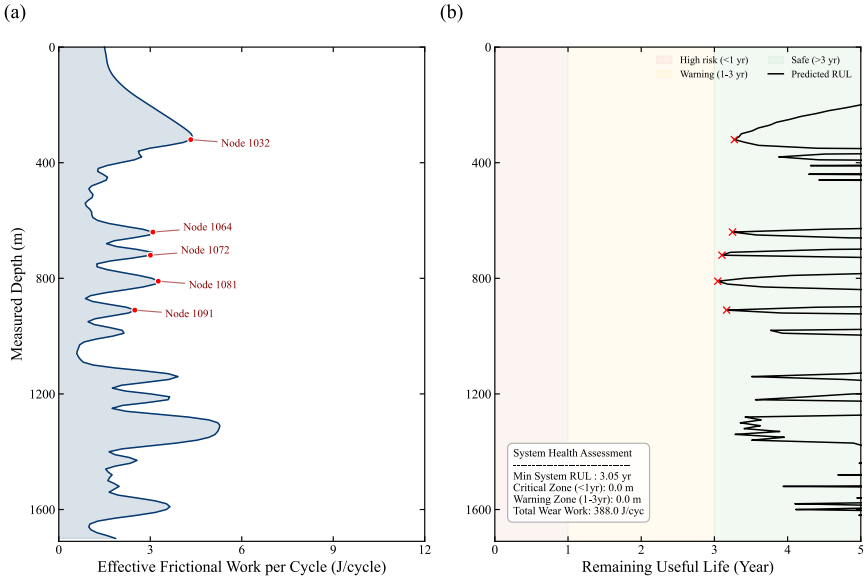


Fig. 18. Wear-distribution and remaining-life estimates for a targeted centralizer-placement scenario. (a) Change in the spatial distribution of frictional work following the geometric modification. (b) Corresponding change in the model-based time to the through-wall criterion under the revised wear formulation.

Figs. 17 and 18. show that the nodes with the shortest predicted life are not entirely identical to the nodes with the maximum absolute frictional work. Due to the smaller sectional modulus and surface area of the 19 mm slender rod sections, their sensitivity to metallic volume reduction is significantly higher than that of the thicker rod sections. Consequently, although the frictional energy dissipation at Node 1076 is slightly lower, its predicted RUL is the lowest across the entire well. Targeted intervention nodes are determined by extracting the local minima from the un-centralized RUL profile.

Based on the baseline wear-risk distribution, candidate locations for discrete centralizer installation are evaluated. In the model, centralizers are represented as geometric standoffs that

modify the local radial clearance and rod–tubing contact geometry. Installing a centralizer changes the local radial clearance from 18.5 mm to 3.5 mm in the configuration considered here. This geometric modification changes the local contact constraints and redistributes the associated normal forces and frictional work. The resulting effect on tubing wear is evaluated using the recalculated contact and wear distributions.

Serving as rigid standoffs, the centralizers not only protect the installation positions but also significantly increase the transverse stiffness of the adjacent rod segments by altering the geometric constraint boundaries. This effectively restricts the high-frequency transverse vibrations and localized dynamic deflection induced by longitudinal stress waves.

To investigate the engineering economics of wear prevention optimization, this paper evaluates centralizer placement schemes for 5, 10, 15, and 20 groups.

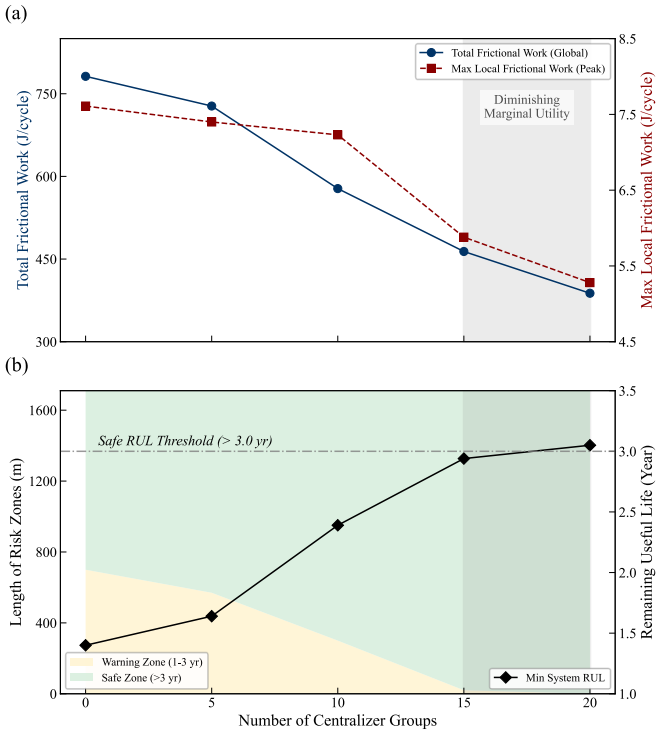


Fig. 19. Sensitivity of system dynamics and tubing reliability to the targeted centralizer placement strategy. (a) Increasing the number of centralizer groups effectively suppresses

both global energy dissipation and localized peak wear intensity. (b) Targeted intervention eliminates the 690 m warning zone and shifts the system into the safe region.

The comparison of the targeted centralizer layouts shows how discrete changes in local clearance and contact constraints influence the computed wear distribution. The model-predicted minimum tubing RUL increases from 1.39 to 2.94 years under the 15-centralizer configuration, further densification to 20 groups yields plateaued lifespan gains.These results provide a case-specific basis for evaluating candidate placements rather than a general guarantee of service-life extension.

5. Conclusions

This study presents a full-scale three-dimensional flexible multibody model for analysing the transient dynamics and wear-prone regions of sucker-rod systems in directional wells. The main conclusions are as follows.

(1) A coupled multibody model was implemented in MBDyn by combining geometrically exact beam dynamics and finite-volume-based spatial discretization with distributed fluid loading, regularized rod–tubing contact and friction, pump loading, and a reduced-order electromechanical drive boundary. Comparison with the measured surface dynamometer card demonstrates that the model reproduces the global load–displacement response of the investigated well.

(2) The simulated stress-wave and contact responses exhibit depth-dependent behaviour associated with wellbore curvature, rod-section transitions, and changes in axial loading. The cumulative frictional-work distribution identifies localized wear-prone regions, including a high-wear region near the recorded tubing-perforation depth. This agreement provides case-specific field corroboration of wear localization.

(3) The constant-voltage and AAVM simulations reveal a competition between changes in macroscopic tensile loading and high-frequency response under delayed voltage feedback. This result is specific to the adopted equivalent electromechanical boundary and voltage-modulation law and should not be interpreted as a direct validation of a particular field-installed drive controller.

(4) Discrete centralizer installation changes the local clearance and contact constraints, which can alter the spatial distribution of contact forces and frictional work. The resulting wear and remaining-life estimates depend on the specified wear relation and physical failure criterion. For the investigated well, the revised framework provides a means to assess candidate centralizer locations under the prescribed operating conditions.

The present work demonstrates how flexible multibody dynamics can link full-well transient mechanical response to case-specific wear assessment. The fluid-loading representation does not explicitly resolve multiphase flow, deposition evolution, or corrosion, and the wear calculation uses field-supplied coefficients under a prescribed operating condition. Accordingly, the results support the analysis of wear-prone locations and the evaluation of modelled intervention scenarios, while broader claims of absolute-life prediction require further independent evidence.

CRediT authorship contribution statement

Yunlong Liu: Conceptualization, Methodology, Software, Validation, Formal analysis, Investigation, Data curation, Visualization, Writing – original draft. **Yanlong Zhao:** Conceptualization, Resources, Writing – review & editing, Supervision, Project administration, Funding acquisition.

Declaration of competing interest

The authors declare that they have no known competing financial interests or personal relationships that could have appeared to influence the work reported in this paper.

Acknowledgments

The authors gratefully acknowledge the financial support from the National Science and Technology Major Project [Grant No. 2025ZD1401503], the National Natural Science Foundation of China [Grant No. 52004301]. Furthermore, the authors would like to acknowledge the developers of the open-source multibody dynamics software MBDyn, which provided the foundational computational framework for this research.

Data Availability

Data will be made available on request.

References

[1] Moreno, G.A., Garriz, A.E., 2020. Sucker rod string dynamics in deviated wells. J. Pet. Sci. Eng. 184, 106534.

[2] Eisner, P., Langbauer, C., Fruhwirth, R.K., 2022. Comparison of a novel finite element method for sucker rod pump downhole dynamometer card determination based on real world dynamometer cards. Upstream Oil Gas Technol. 9, 100078.

[3] Li, Z., Fang, F., Lu, H., Han, J., Li, Y., Yang, S., 2025. Analysis of sucker rod partial wear based on COMBIN40 element equivalence. Results Eng. 27, 105576.

[4] Jiang, J., Wan, X., Li, K., Du, J., Liu, Y., Jing, J., Li, J., 2024. Research progress of sucker rod fracture detection and prediction model. Eng. Fail. Anal. 159, 108119.

[5] Lv, X., Wang, H., Liu, Y., Chen, S., Lan, W., Sun, B., 2020. A novel method of output metering with dynamometer card for SRPS under fault conditions. J. Pet. Sci. Eng. 192, 107098.

[6] Wang, X., Lv, L., Li, S., Pu, H., Liu, Y., Bian, B., Li, D., 2021. Longitudinal vibration analysis of sucker rod based on a simplified thermo-solid model. J. Pet. Sci. Eng. 196, 107951.

[7] Wu, F., Zhao, K., Wu, X., Peng, H., Zhao, L., Zhong, W., 2024. A time-averaged method to analyze slender rods moving in tubes. Int. J. Mech. Sci. 279, 109510.

[8] Lv, X., Wang, H., Zhang, X., Liu, Y., Chen, S., 2021. An equivalent vibration model for optimization design of carbon/glass hybrid fiber sucker rod pumping system. J. Pet. Sci. Eng. 207, 109148.

[9] Shabana, A.A., 1997. Flexible Multibody Dynamics: Review of Past and Recent Developments. Multibody Syst. Dyn. 1, 189–222.

[10] Simo, J.C., 1985. A finite strain beam formulation. The three-dimensional dynamic problem. Part I. Comput. Methods Appl. Mech. Eng. 49, 55–70.

[11] Bauchau, O.A., Trainelli, L., 2003. The natural parameterization of rigid body motion and its application to flexible multibody dynamics. Multibody Syst. Dyn. 8, 1–24.

[12] Lang, H., Linn, J., Arnold, M., 2011. Multibody dynamics simulation of geometrically exact Cosserat rods. Multibody Syst. Dyn. 25, 285–312.

[13] Kinon, P.L., Eugster, S.R., Betsch, P., 2026. Mixed formulation and structure-preserving discretization of Cosserat rod dynamics in a port-Hamiltonian framework. Comput. Methods Appl. Mech. Eng. 458, 118966.

[14] Xun, L., Tamadazte, B., 2026. Geometrically explicit cosserat-rod modeling with piecewise linear strain for complex rod systems. Comput. Struct. 325, 108181.

[15] Zanella, A., Abergo, L., Caccia, F., Morelli, M., Guardone, A., 2023. Towards an open-source framework for Fluid–Structure Interaction using SU2, MBDyn and preCICE. J. Comput. Appl. Math. 429, 115211.

[16] Zhang, W., Wang, J., Guo, H., Liu, Y., Wan, D., 2025. Numerical investigations of ship hydroelasticity of a 20,000 TEU containership based on CFD-MBD method. Ocean Eng. 317, 120061.

[17] Leng, J., Li, G., Duan, L., 2025. Complex dynamics of downwind floating offshore wind turbines due to towe shadow and platform motions. Energy 328, 136378.

[18] Xu, K., Feng, Z., Jiang, C., Dong, Y., Jiang, Y., Zhang, R., Zuo, W., 2025. Nonlinear mechanical behavior and dynamic analysis of small-module helical belts. Int. J. Mech. Sci. 305, 110807.

[19] Li, B., Wang, X., Masarati, P., Xu, Y., 2025. A novel modeling framework for tiltrotor coupled drivetrain dynamics. Chinese Journal of Aeronautics 38, 103666.

[20] Tan, C., Feng, Z.M., Liu, X., Fan, J., Cui, W., Sun, R., Ma, Q., 2020. Review of variable speed drive technology in beam pumping units for energy-saving. Energy Rep. 6, 2676–2688.

[21] Yang, S., Zhu, C., Li, C., Zhou, Y., Tan, J., Liao, B., 2025. Physics-data hybrid dynamic analysis of novel integrated wind turbine drivetrain. Int. J. Mech. Sci. 302, 110564.

[22] Sawaryn, P.I., Thorogood, J.L., 2005. A compendium of directional calculations based on the minimum curvature method. SPE Drill. Complet. 20, 24–36.

[23] Bauchau, O.A., Trainelli, L., 2003. The vectorial parameterization of rotation. Nonlinear Dyn. 32, 71–92.

[24] Masarati, P., 2014. On the choice of the reference frame for beam section stiffness properties. Int. J. Solids Struct. 51, 2439–2447.

[25] Ghiringhelli, G.L., Masarati, P., Mantegazza, P., 2001. Analysis of an actively twisted rotor by multibody global modeling. Composite Structures 52, 113–122.

[26] Linn, J., Lang, H., Tuganov, A., 2013. Geometrically exact Cosserat rods with Kelvin–Voigt type viscous damping. Mech. Sci. 4, 79–96.

[27] Shooshtari, A., Khadem, S.E., 2006. Non-linear free vibrations of Kelvin–Voigt visco-elastic beams. Int. J. Mech. Sci. 48, 1161–1168.

[28] Lubinski, A., Althouse, W.S., Logan, J.L., 1962. Helical buckling of tubing sealed in packers. J. Pet. Technol. 14, 655–670.

[29] Lankarani, H.M., Nikravesh, P.E., 1990. A contact force model with friction in multibody mechanical systems. J. Mech. Des. 112, 369–376.

[30] Brown, P., McPhee, J., 2016. A continuous velocity-based friction model for dynamics and control with physically meaningful parameters. J. Comput. Nonlinear Dyn. 11, 054502.

[31] Gibbs, S.G., 1963. Predicting the behavior of sucker-rod pumping systems. J. Pet. Technol. 15, 769–778.

[32] Hogan, N., 1985. Impedance control: An approach to manipulation: Part I—Theory. J. Dyn. Syst. Meas. Control 107, 1–7.

[33] Ibrahim, R.A., 1994. Friction-induced vibration, chatter, squeal, and chaos: Part I—Mechanics of contact and friction. Appl. Mech. Rev. 47, 209–226.

[34] Mitchell, R.F., 1988. New concepts for helical buckling. SPE Drill. Eng. 3, 303–310.

[35] Hutchings, I.M., Shipway, P., 2017. Tribology: Friction and Wear of Engineering Materials, second ed. Butterworth-Heinemann, Oxford.